Development of nanoparticle catalysts and total internal reflection (TIR) Raman spectroscopy for improved understanding of heterogeneous catalysis

BINGHAM, LAURA,MARIA

Chapter 3. Nanoparticle synthesis, deposition, and initial studies by confocal and TIR Raman

This chapter demonstrates the synthesis of small, size controlled nanoparticles of varying compositions (Chapter 1, Sections 1.5, 1.6). Subsequent deposition onto suitable substrates (carefully selected to reduce fluorescent effects in Raman studies) was achieved using Langmuir Blodgett (LB) techniques. Finally, confocal and then TIR Raman were used, as initial proof of concept of the increased sensitivity of TIR Raman to surface bound species. The applicability of this technique to the study of surface species (*e.g.* intermediates, adsorbates) for heterogeneous catalysis has been investigated using synthetic templating agents bound to nanoparticle surfaces as model adsorbates.

3.1. Nanoparticle synthesis, for use in initial TIR Raman experiments

Nanoparticles typical of those used in catalysis experiments with several different metals and different widely used capping agents were synthesised. All were suitable for use as part of a uniform catalyst film, prepared by using LB techniques (Chapter 3, Section 3.2). Single layers of uniform nanoparticle films formed by LB deposition are important in the overall goal of the project as they afford easy access of gas phase molecules to the nanoparticle surfaces (not necessarily true of drop casting). This issue of reagent access is necessary for *in situ* catalytic experiments using TIR Raman (Section 1.4). For this purpose, the synthesis of small, monodisperse particles, with a uniform particle shape, was desired in order to achieve the desired uniform particle film. Uniform particles also allow us to monitor, before and after the experiment, for changes in the sample, for instance by scanning electron microscopy (SEM).

Transmission electron microscopy (TEM) was primarily used for assessment of the as synthesised nanoparticles, enabling determination of mean particle size and the uniformity or particle size distribution present. Results for a variety of nanoparticle systems are detailed within this section. In addition, for nanoparticles where two capping agents were present Fourier Transform infrared (FTIR) analysis was used to try and elucidate which species remain on the surface of the nanoparticles prior to studies with Raman spectroscopy (Section 3.1.2.2).

3.1.1. Platinum/polyvinylpyrrolidone nanoparticles (platinum/PVP nps) for proposed use as a hydrogenation catalyst

3.1.1.1. TEM imaging

As discussed in the introduction (Section 1.6.3), platinum has many applications, including as a catalyst in organic reactions, such as hydrogenation.[1–4] Platinum/polyvinylpyrrolidone nanoparticles (platinum/PVP nps) were synthesised by the widely used polyol method, since this system has perhaps been most widely used in catalysis. TEM data (Figure 3.1) confirmed the intended synthesis of small, uniformly-sized nanoparticles. The images obtained show very little evidence of agglomeration, and so the particles prepared here are expected to give the desired uniform films for studies by TIR Raman. Any aggregation apparent on the sample is indistinguishable from particles that are next to one another on the TEM grid film and this may be a result of the particle deposition and drying during preparation of the TEM sample. The average particle size obtained (4.2 nm) from the TEM images was close that reported by Krier *et al.,*[5] from whom the synthesis was taken.

In Figure 3.1 B it is noticeable that the TEM image of the platinum nanoparticles contain Moiré patterns or fringes (identified in red in the figure). These distinct coarse lines are due to either overlapping platinum particles, platinum particles that contain multiple crystals, or platinum nanoparticles that contain dislocations in their crystal structure.[6] Lattice fringes were also seen and are identified in blue in Figure 3.1 B. features were observed due to the similarity of wavelength of the electrons in the microscope, to the lattice spacing of the platinum. Lattice fringes are features which arise due to the interference of Bragg diffracted electron waves. Whether a lattice fringe can be seen depends upon the coherence, as well as the stability of the microscope. Where coherence is an ideal property of the wave, which allows stationary interference of the electron wave.[7] Lattice fringes are important as they provide information on lattice spacing and orientation. Accordingly lattice fringes are often only observed in certain orientations. The presence of lattice fringes provides an insight into the crystallinity of the materials, confirming their crystalline nature.

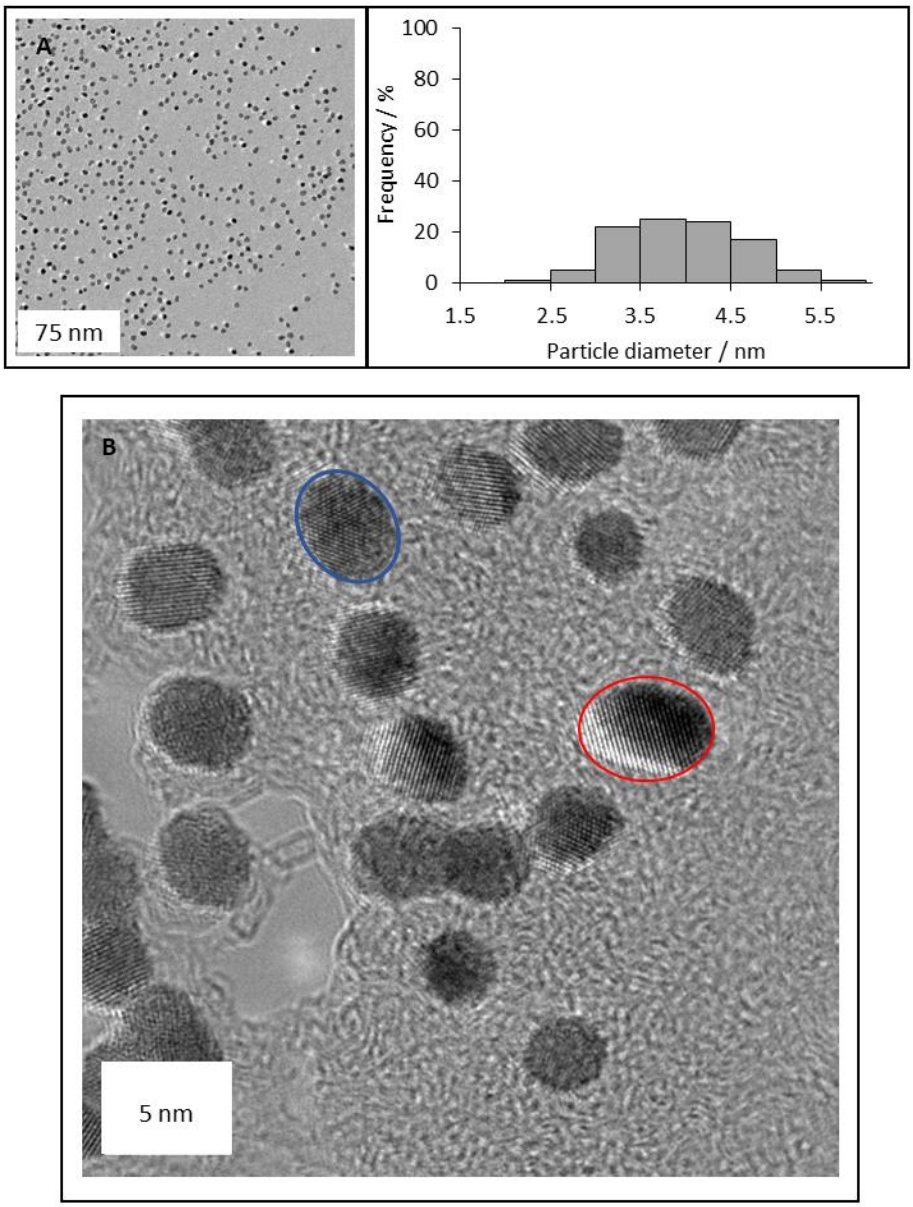

Figure 3.1. A) (left) Typical TEM image of as synthesised platinum/PVP nps (prepared as outlined in Chapter 2, Section 2.2.1.1), (right) corresponding particle size distribution (4 ± 1 nm) obtained from multiple images of this sample. B) shows region of image at higher resolution, with both lattice fringes (blue) and Moiré patterns (red) seen.

3.1.2. Silver/oleylamine/oleic acid nanoparticles (silver/OAm/OAc nps) for proposed use as an epoxidation catalyst

Silver nanoparticles were synthesised from silver perchlorate, using both oleylamine and oleic acid (silver/OAm/OAc nps) in combination as capping agents, by the method detailed in Section 2.2.1.4. As discussed in the introduction, silver finds a role in a number of catalytic processes, and these nanoparticles are of the type expected to be used in the investigation of catalytic reactions such as epoxidation. Here, I have prepared them for application in TIR Raman studies.

The method used was based on Koski *et al*.,[8] and one variable explored here was the impact of ripening time – the length of time between the start and end of the particle nucleation and growth periods. Ripening time was varied (either 2 min or 1 h), to allow optimisation of the standard preparation. It was expected that the longer ripening time would allow access to a narrower particle distribution *via* a ripening mechanism. If the system follows Ostwald type growth then it might be expected that longer ripening would also give larger particles.[9]

3.1.2.1. TEM imaging

TEM images and particle size data for particles produced using 2 min and 1 h ripening times are shown in Figure 3.2 A and 3.2 B respectively. As for the platinum case above, using the reported procedure no significant agglomeration was seen for either sample. In contrast to the expectation from Ostwald type growth, no significant change in particle size was seen as ripening time was varied. This might suggest a system that rapidly reaches a quasi-equilibrium particle size distribution or in which another ripening mechanism is present (phenomena that will be explored in more detail for copper in the subsequent chapter).

The optimum ripening time, to be used for standard preparations, could not clearly be deduced. The 1 h ripening time was selected, to ensure the equilibrium size distribution was achieved. This was of particular importance in cases where other experimental parameters were varied.

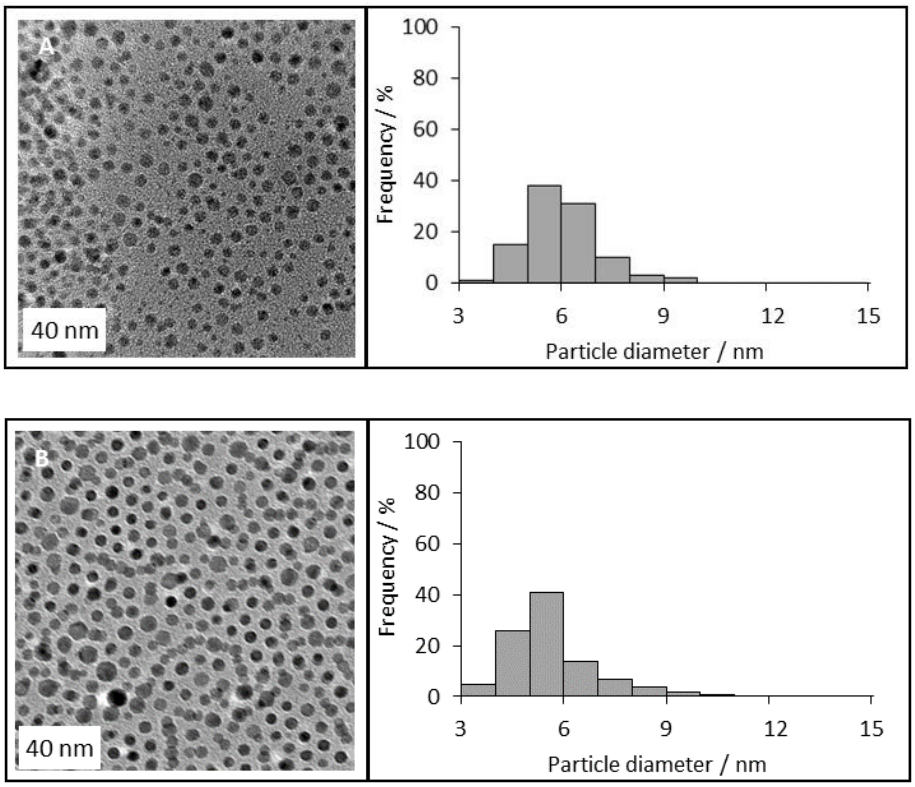

Figure 3.2. (left) Typical TEM images of as synthesised silver/OAm/OAc nps with A) 2 min and B) 1 h ripening times (prepared as outlined in Section 2.2.1.4), (right) corresponding particle size distribution (6 ± 1 nm for both data sets) obtained from multiple images of this sample.

The quantity of capping agent was also anticipated to be an important variable and so the synthesis of the silver nanoparticles was repeated with the molar ratio of oleylamine:oleic acid halved from 2:1 to 1:1. A 1 h ripening time was used. Furthermore this change was investigated with the goal of simplifying the FTIR spectroscopy study detailed later (Section 3.1.2.2). TEM images of this sample and the corresponding size distribution are given in Figure 3.3. The average particle size was broadly similar to that of particles synthesised with the 2:1 molar ratio of oleylamine:oleic acid, although the distribution was centred towards a slightly larger particle size. It might be expected that a reduced amine concentration would lead to a larger particle size as the primary function of the capping agent is to inhibit particle growth. As smaller particles have a greater surface area, they should require larger quantities of capping agent in order to provide sufficient stabilisation of the nanoparticle size. This would correspond with the slightly larger particle size seen.

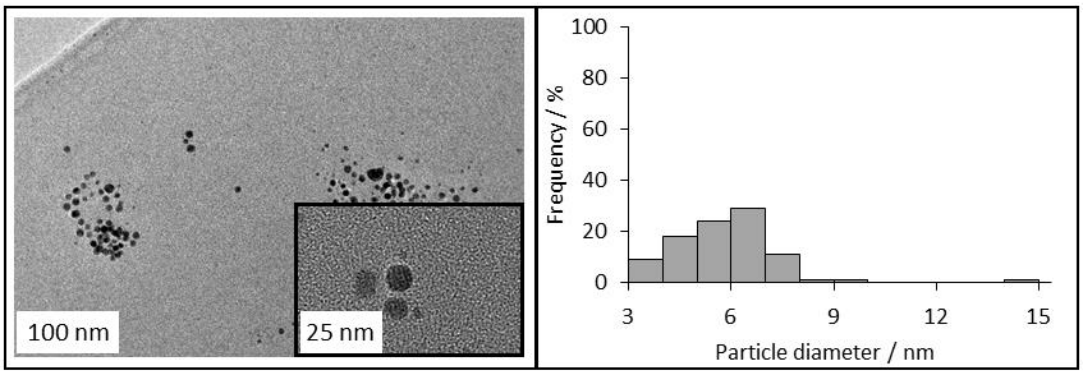

Figure 3.3. (left) Typical TEM image of as synthesised silver/OAm/OAc nps with a 1:1 molar ratio of oleylamine:oleic acid (prepared as outlined in Section 2.2.1.4), (right) corresponding particle size distribution (6 ± 2 nm) obtained from multiple images of this sample.

3.1.2.2. Investigation of the nature of the capping agent for silver/OAm/OAc nps

For the synthesis of silver nanoparticles two capping agents were used. Oleylamine was present throughout the synthesis. Oleic acid was added after ripening of the nanoparticles. This method was used in the procedure on which the synthesis was based, where it was proposed that oleic acid displaces the oleylamine and binds irreversibly, resulting in a defined end to particle growth.[8] This proposal was due to the stronger interaction of the metal with the acid functional group than with the amine. It was, however, unclear if oleylamine would be fully displaced by oleic acid and no evidence was given for this occurring or whether it occurred completely. For the subsequent TIR Raman studies it is of interest to know which species are on the surface, as one or both capping agents could dominate at the surface of the metal nanoparticle. FTIR analysis of a bulk sample was therefore performed to determine the nature of the capping agent. Figure 3.4 Spectra 1 and 2 were obtained for the as synthesised silver nanoparticle samples with two acid:amine capping agent ratios. In a typical silver nanoparticle synthesis the molar ratio of silver to capping agent for silver:oleylamine:oleic acid was 1:2:1. However, 1:1 binding of the silver to capping agent was likely to represent an upper limit. This is because some atoms will be buried below the nanoparticle surface, and steric crowding may not permit the surfactant to access evenly all of the available surface sites. Therefore, in order to identify the majority species remaining in the supernatant (an important objective as discussed below), it was more instructive to begin with a 1:1 ratio of oleic acid to oleylamine and so the 1:1 ratio was used despite the

slightly lower degree of control seen above Section 3.1.2.1 Figure 3.3. It was calculated that this would still provide full coverage of the silver nanoparticle surface (see Appendix).

The FTIR spectral quality was poor (for both acid:amine ratios) and the signal to noise ratio was low. In particular this permitted poor discrimination of features in the range 500 cm^{-1} to 1400 cm^{-1}. Although three bands were seen: ν_{as}(C-H) and ν_{s}(C-H) vibrational modes at 2920 and 2850 cm^{-1} respectively,[10] as well as a strong band centred around 1500 cm^{-1} which could be assigned to either oleic acid as a complex mix of ν_{s}(C-C), ν_{s}(C-O), CH_2 def,[11] or to oleylamine as $\delta(CH_3)$.[10]

Spectra were recorded for the supernatant species (for preparations using both acid:amine capping ratios) obtained during purification by precipitation and centrifugation of the reaction mixture (Figure 3.5, Spectra 1 and 2). For the supernatant spectra hexane solvent was removed, by rotary evaporation, prior to running FTIR analysis. This might be expected to yield some slight improvement in spectral quality, and reduce the appearance of unnecessarily intense solvent peaks. This could not be done for the nanoparticle solution, as rotary evaporation was expected to induce agglomeration or degradation of the nanoparticles. From the supernatant spectra a number of features were resolved and were assigned using expected literature values (Tables 3.1 and 3.2). Reference spectra (Figure 3.6) were also acquired for both capping agent molecules in the pure form and the data obtained is in agreement with the literature.[10–12] However, even with this reference spectrum it was difficult to distinguish which species was predominantly present in the supernatant species. Metal salt reduction takes place during the early stages of nanoparticle synthesis so does so under basic conditions. Correspondingly the effect of basicity upon the two capping agents was explored with FTIR spectra recorded for both capping agents under both acidic and basic conditions (Figure 3.7, Spectra 1-4). It was hoped this would allow determination of whether protonation/deprotonation might have taken place for the amine and acid function groups present in the oleylamine and oleic acid capping agents respectively. These spectra were then used to aid assignment of the supernatant FTIR spectra. It was seen that the basic oleylamine and oleic acid gave the closest replication of the supernatant spectra. This was in-line with the expected basicity of the nanoparticle solution during the early stages of particle nucleation and growth. However, there was still particular difficulty in deducing which of the two capping agents was predominantly present in the spectra recorded for the nanoparticle supernatant species (or indeed in the spectra recorded for the originating nanoparticle solution). This gave a number of possible explanations consistent with the spectra recorded. Firstly, both of the capping agents were bound to the metal surface of the

nanoparticle. Secondly, it maybe that (given a 1:1 silver to capping agent ratio represented the upper limit of capping agent bound to metal, see Appendix), the amount of capping agent was actually a substantial excess and so large quantities of both remain present in the supernatant.

One further observation was that some of the spectral features seen for the supernatant material (centred at 630, 820, and 1100 cm^{-1}) were absent from both the nanoparticle and capping agent spectra. One possible assignment is to synthetic agents such as 1,2 tetradecanediol and perchlorate (from silver perchlorate) which were present during the synthesis. For 1,2 tetradecanediol IR bands would be expected at 1466, and 1075 cm^{-1}.[13,14] For the perchlorate, an approximation of the anticipated IR frequency, can be given from the similar compound ammonium perchlorate. For ammonium perchlorate IR bands were expected in the region of 954-1060 cm^{-1}.[15] Therefore these species could fit with some, but not all of the previously unassigned spectral features. One further possibility was that complexation of oleylamine and metal could occur in the absence of reduction. This would not produce nanoparticles but could result in other spectroscopic signals. Moreover, it is difficult to predict the IR stretching frequency of such a complex. Overall, the direct determination of the capping agent composition for the nanoparticle or supernatant by FTIR was not possible, although it appears likely that some of both capping agent species were present in the nanoparticle supernatant.

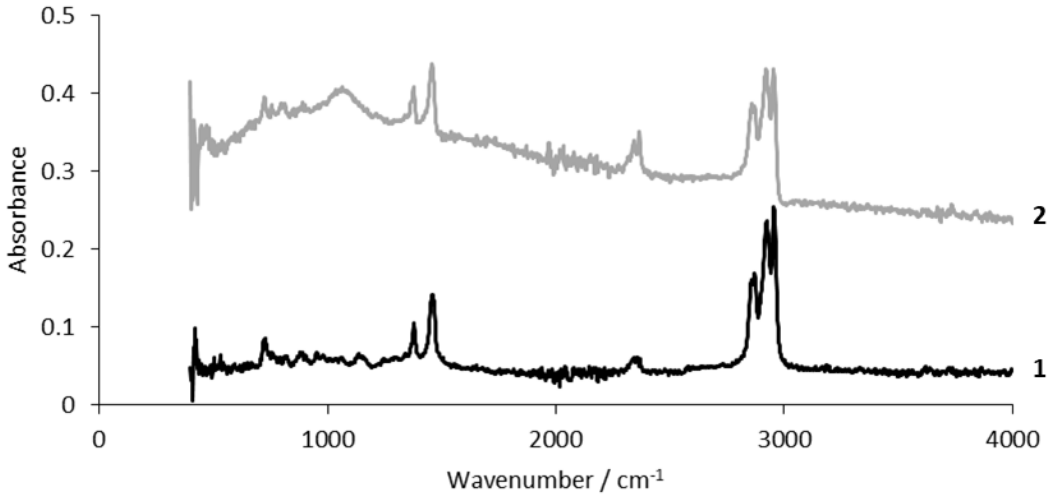

Figure 3.4. FTIR spectra of silver/OAm/OAc nps synthesised with 1- 1:1, and 2- a 2:1 molar ratio of oleylamine:oleic acid. Spectra been offset vertically for clarity.

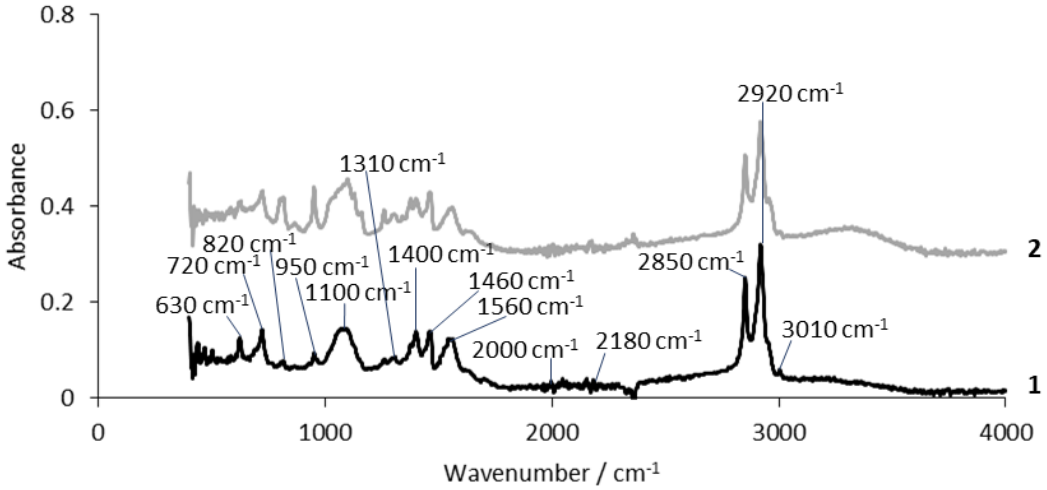

Figure 3.5. FTIR spectra of supernatant from silver/OAm/OAc nps, synthesised with a molar ratio of oleylamine:oleic acid of 1- 1:1, and 2- 2:1. Spectra been offset vertically for clarity.

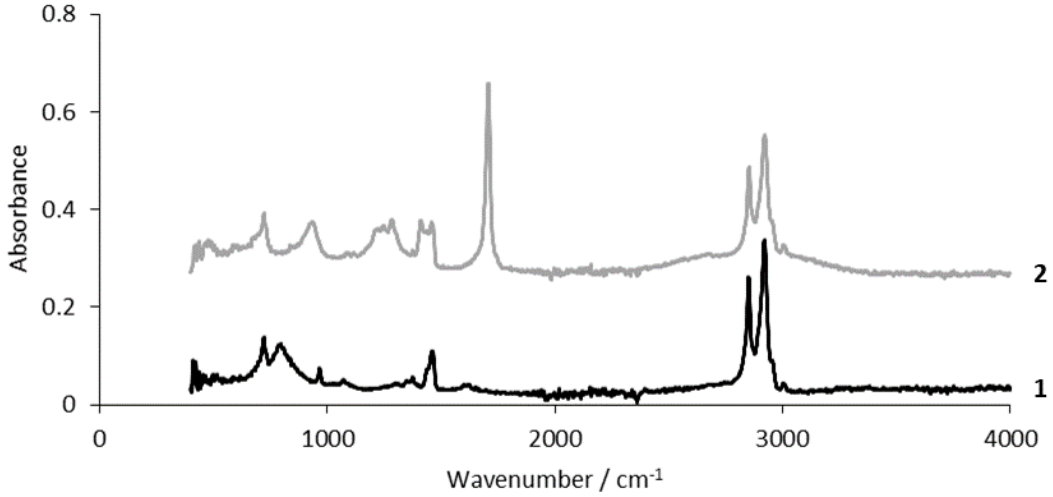

Figure 3.6. FTIR spectra of 1- oleylamine capping agent (as purchased), and 2- oleic acid capping agent (as purchased). Spectra been offset vertically for clarity.

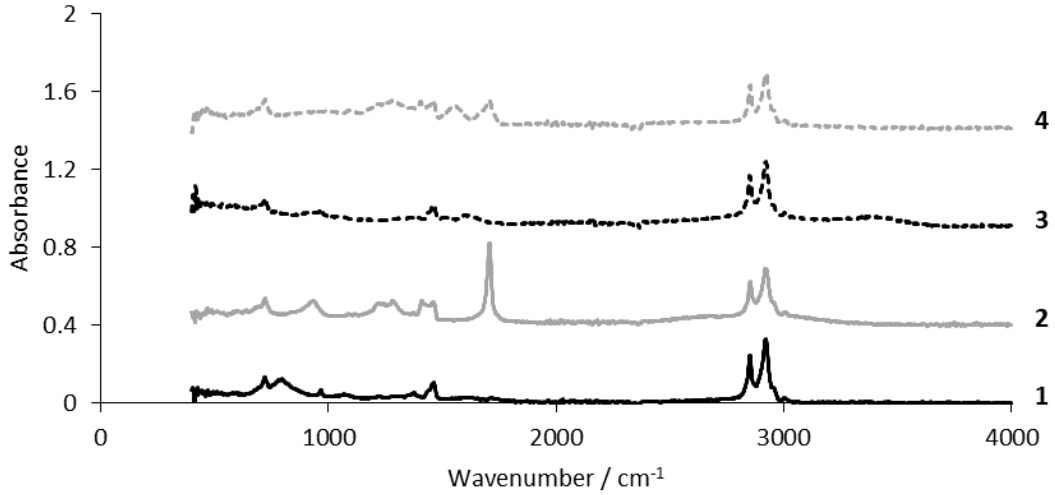

Figure 3.7. FTIR spectra of: 1- oleic acid with sodium hydroxide pH 9, 2- oleic acid with hydrochloric acid pH 1-2, 3- oleylamine with hydrochloric acid (which formed a gel), and 4- oleylamine with sodium hydroxide pH 7-8. Spectra been offset vertically for clarity.

Table 3.1. Table to show expected literature bands and assignments for capping agents oleylamine (OAm)[11,12] *and oleic acid (OAc).*[10,11] *Where vs = symmetric stretching vibration, vas = asymmetric stretching vibration, def= deformation, δ = bending vibration.*

Literature vibrational mode	**Frequency / cm^{-1}**
OAc	
Complex mix: vs(C-C), vs(C-O), CH_2 def[11]	Around 1500
vs(C=C)[11]	1648
vsC=O[12,11]	1710
vs(O-H)[11]	2670
vs(CH_3), (CH_2)[12]	2800-3000
vs, vas(CH_2)[11]	2854, 2922
vs(C-H)[11]	3006
vs(=C-H)[12]	3025
OAm	
vs(C-C)[10]	722
vs(C-N)[10]	1071
δ(CH_3)[10]	1465
δ(NH_2)[10]	1604, 795
vs(C=C)[11]	1647
vas(C-H) and vs(C-H)[10]	2925, 2853
vs (=C-H)[10]	3004
vs(N-H)[11]	3300
vas(NH_2) and vs(NH_2)[10]	3376, 3295

Table 3.2. Table to show assignment of bands seen in the FTIR spectra ran for the supernatant of silver/OAm/OAc nps (Figure 3.5), synthesised with oleylamine (OAm) and oleic acid (OAc) capping agents, [10–12] with a molar ratio of the capping agents of oleylamine:oleic acid of 1:1. Assignment for the supernatant of silver nanoparticles, synthesised with a molar ratio of the capping agents of oleylamine:oleic acid of 2:1, was identical and so was not shown. Where vs = symmetric stretching vibration, vas = asymmetric stretching vibration, def= deformation, δ = bending vibration.

Assigned Vibrational mode	**Frequency / cm^{-1}**
unassigned	630, 950, 1310, 1400, 2000, 2180
OAc	
Complex mix: vs(C-C), vs(C-O), CH_2 def[11]	1460, 1560
vas(CH_2)[11]	2920
vs(CH_2)[11]	2850
vs(C-H)[11]	3010
OAm	
vs(C-C)[10]	720
δ(NH_2)[10]	820
vs(C-N)[10]	1100
δ(CH_3)[10]	1460
δ(NH_2)[10]	1560
vas(C-H) and vs(C-H)[10]	2920, 2850
vs(=C-H) [10]	3010

3.1.2.2.1. TEM analysis of silver nanoparticle supernatant

The supernatant solution typically obtained during nanoparticle purification was colourless, however, on rotary evaporation of the reaction solvent a dark brown/black coloured gel resulted. This was similar in colour to the primary nanoparticle product. Nanoparticle colour is an important property, and can often give an indication not only of successful nanoparticle formation, but also of properties such as particle size.[16–19] It was, therefore, suspected that small amounts of nanoparticle material may have been present in the supernatant. This could have an impact upon the validity of the FTIR results, given above in Section 3.1.2.2.

TEM of the supernatant gel dispersed in a hexane was recorded as shown in Figure 3.8, and confirmed the presence of particles in the supernatant. Energy Dispersive X-ray (EDX) analysis (Figure 3.9) confirmed the particles also contain silver. It should be noted that the carbon and copper seen in the EDX spectra, originate from the TEM grid. Silicon was also seen, and was likely to be due to traces of silica grease used to give a vacuum seal during the inert preparation. The particles in the supernatant (Figure 3.8) were noticeably smaller in size than those in the product solution (Figure 3.3, Section 3.1.2.1). The reduction in size, might suggest the difficulty of washing very small particles, due to inability of the solvent and anti-solvent system used to precipitate sufficiently heavy solids for centrifuging. Indeed, this has been used as an approach for obtaining size selected nanoparticles, although with low yield.[20,21] This highlights the importance of careful selection of solvents for nanoparticle washing and the importance of this step in obtaining adequate overall yields (in later sections of the thesis inductively coupled plasma-optical emission spectrometry (ICP-OES) yields were obtained to address this point specifically). The clear presence of some nanoparticles in the supernatant solutions should be considered in interpreting the IR data above, although as no clear conclusions as to the composition of the solutions were reached this is just an additional complication that should be borne in mind in future studies.

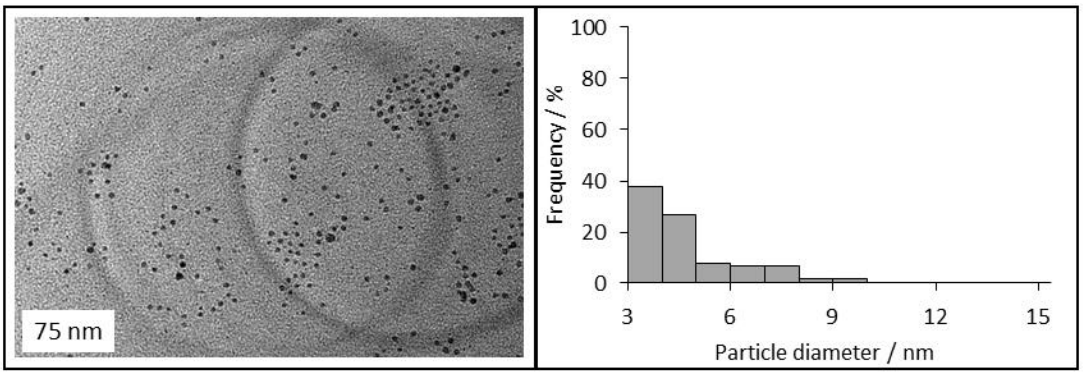

Figure 3.8. (left) Typical TEM image of as supernatant for synthesised silver/OAm/OAc nps with a 1:1 molar ratio of oleylamine:oleic acid and 1 h ripening time (prepared as outlined in Section 2.2.1.4), (right) corresponding particle size distribution (5 ± 2 nm) obtained from multiple images of this sample.

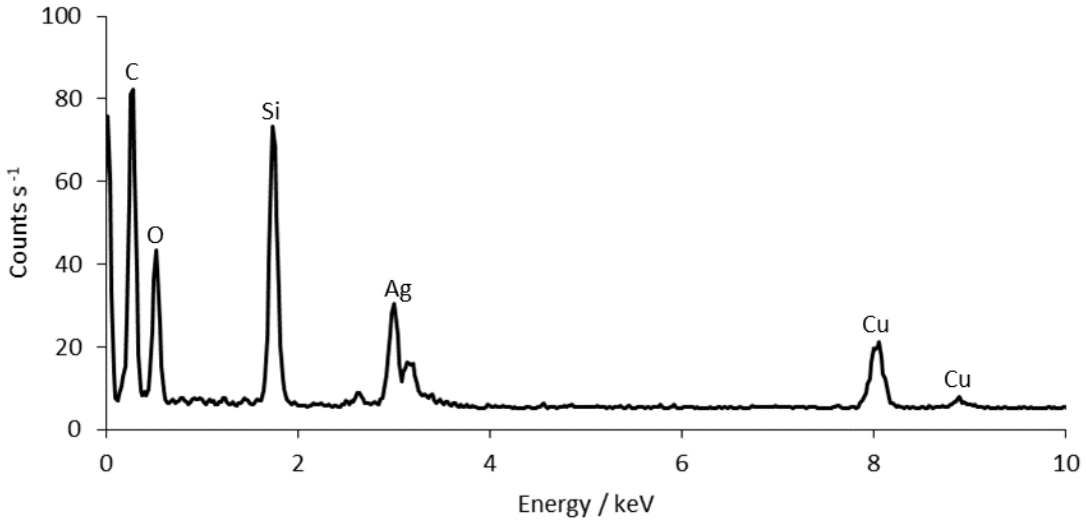

Figure 3.9. EDX chemical analysis taken for supernatant of silver/OAm/OAc nps synthesised according to Section 2.2.1.4 with a 1 h ripening time and a 1:1:1 silver: oleylamine: oleic acid, molar ratio.

3.1.3. Palladium/oleylamine nanoparticles (palladium/OAm nps)

As detailed in the introduction palladium nanoparticles are of interest for various catalytic applications, in particular hydrogenation, oxidation and C-C coupling. They are therefore of interest to investigate the feasibility of studying using TIR Raman spectroscopy. Palladium nanoparticles were synthesised from palladium(II) acetylacetonate, with an oleylamine capping agent, as detailed in Section 2.2.1.8. This capping agent system was selected based on a literature review of possible syntheses and my initial TIR Raman results for platinum/PVP and silver/OAm/OAc nps, which suggested that the oleylamine capped and oleylamine and oleic acid dual capped nanoparticles displayed lower levels of fluorescent background (Section 3.5 and 3.6). This is important in Raman spectroscopy as explained in the methodology as fluorescence masks spectral features resulting from Raman Scattering.

The silver nanoparticle system described above uses two capping agents which complicates the possible final structure and so for palladium nanoparticles if adequate size control could be achieved using oleylamine only, this could lead to simplification of the TIR Raman spectra obtained. Oleylamine capped palladium nanoparticles (palladium/OAm nps) were characterised by TEM imaging as shown in Figure 3.10. The as synthesised particles showed little agglomeration, but exhibited a slightly broader particle size distribution as compared to the silver/OAm/OAc nps discussed above. Nevertheless this slightly broader distribution and the <10 nm size achieved for palladium produced particles was suitable for production of the desired uniform catalyst film for the TIR Raman experiment.

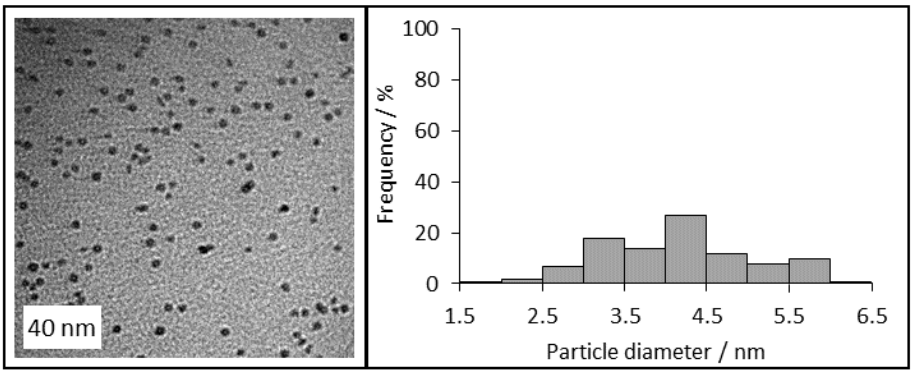

Figure 3.10. (left) Typical TEM image of as synthesised palladium/OAm nps (prepared as outlined in Section 2.2.1.8), (right) corresponding particle size distribution (4 ± 1 nm) obtained from multiple images of this sample.

3.1.4. Investigation of oleylamine capping agent purity

Technical grade oleylamine (70% purity) is widely used in nanoparticle synthesis, without much consideration as to the impact of the purity upon its role as a capping agent. The structure of the amine is known to be important. Other alkylamines such as dodecylamine, or hexadecylamine, substituted in the place of oleylamine, have been reported to not produce monodisperse nanoparticles.[22–25] Hence it was suspected that the alkene functionality in oleylamine was crucial in stabilising nanoparticle formation and producing a narrow size distribution.[26] To further exemplify the issue, Lablokov *et al*. stated that repeatable results could not be achieved using technical grade oleic acid.[27] In order to allow accurate control of nanoparticle properties, including particle size and shape, the nature and composition of the capping agent and any impurities present within it needs to be known.

gas chromatography – mass spectrometry (GCMS) was recorded for the as obtained oleylamine (supplied from Acros organics, approximate 80-90% C_{18} content). Assignments were made as follows for the following retention times: 18.5 min, $C_{16}H_{31}NH_2$, m/z EI 30 (100%), 55 (17), 69 (7), 114 (5), 154 (7), 182 (2), 239 (M+, 1). 18.7 min, $C_{16}H_{33}NH_2$, m/z EI 30 (100%), 44 (16), 86 (6), 114 (1), 142 (1). 20.6 min oleylamine peak 30 (100%), 55 (32), 56 (19), 114 (11), 140 (5), 154 (21), 168 (7), 196 (1), 224 (1), 267 (2). 20.6 min, oleylamine shoulder, m/z EI 30 (100%), 55 (19), 69 (9), 95 (6), 110 (2), 154 (7), 182 (3), 210 (1), 267 (1).

The compounds in the GCMS were assigned as oleylamine ($C_{18}H_{35}NH_2$) and two lower weight fractions $C_{16}H_{33}NH_2$ and $C_{16}H_{31}NH_2$.[28] The splitting of the oleylamine peak (assigned above as oleylamine shoulder) might be attributed to cis/trans isomerisation. In order to prove this, oleylamine could be hydrogenated with a suitable heterogeneous catalyst. The hydrogenated product of oleylamine should no longer have cis/trans isomers (due to removal of the C=C bond) and so only one oleylamine peak should be obtained by GCMS. If

more than one peak is obtained then the original splitting was not due to cis/trans isomers. Due to not being key to the main goals of the project this was not pursued further, but could be considered in the future if it might contribute to spectral assignment.

In order to explore the impact of the impurities identified by GCMS, some oleylamine was purified to try and remove the C_{16} fractions using vacuum distillation. Assignments were made as follows for the following retention times: 18.5 min, $C_{16}H_{31}NH_2$, m/z EI 28 (100%), 30 (43), 32 (32), 41 (8), 67 (5), 95 (3), 126 (1), 154 (3), 182 (1). 18.7 min, $C_{16}H_{33}NH_2$, m/z EI 28 (100%), 32 (33), 44 (15), 86 (7), 114 (1), 142 (1). 20.5 min oleylamine peak, m/z EI 30 (100%), 41 (22), 56 (11), 95 (8), 140 (4), 154 (14), 182 (4), 224 (1), 267 (1). 20.6 min oleylamine shoulder, m/z EI 30 (100%), 32 (25), 67 (11), 95 (7), 109 (3), 154 (7), 182 (4), 210 (1), 267 (1). Two fractions were removed, water at 80 °C, and a further fraction at 100 °C presumed (by GCMS) to be $C_{16}H_{31}NH_2$ and $C_{16}H_{33}NH_2$. However, not all of the C_{16} fractions were removed. A very approximate estimate of the effect of distillation can be gained from direct inspection of the relative area under the C_{16} peaks in the GCMS trace. A small decrease in the peak area was seen for the smaller weight fractions. Hence further vacuum distillation, would be required, to remove the rest of the lower weight fractions. While this approach might be viable it did not yield a quick purification of the oleylamine and this was not pursued further as not central to the project.

The difficulty in either characterising or purifying the other fractions present in commercially available oleylamine perhaps explains the widespread use of the unpurified form in nanoparticle synthesis, but does not remove some of the challenges discussed above. Interestingly the saturated species octadecylamine is a crystalline material and so is available in much higher purity. In Chapter 4 on copper nanoparticle synthesis both are used comparatively and the above assertion from the literature on the necessity of the unsaturated C=C bond did not appear to hold true, possibly due to the greater purity of one of the two capping agents.

3.2. LB trough deposition, of nanoparticles onto silicon wafers and silica hemispheres for bulk and TIR Raman spectroscopy

Once the desired small and monodisperse nanoparticles had been synthesised, they could be deposited onto the reflection element used in the TIR Raman experiment, in our case a clean silica hemisphere. This would allow for formation of the catalyst surface on the flat face of the hemisphere (nanoparticle material was removed from the curved surface), and the TIR Raman scattered light was then detected at the back through the curved

hemispherical face (as described in Section 2.1.5.4). In order to deposit films one monolayer of nanoparticles deep a LB technique was developed. This technique was chosen, to allow for the formation of close packed thin surfaces, in order to provide a uniform, densely packed catalyst surface. Monolayer samples were required to give particles near enough the silica/air interface to be within the TIR probing distance and to ensure for *in situ* experiments good contact between gas and nanoparticles (as no nanoparticles are buried under other layers of material). An explanation of the fundamentals, and theory behind this approach can be found in methodology Section 2.1.5.4 In this section the LB deposition of nanoparticles systems described in Section 3.1 is discussed.

3.2.1. Platinum/PVP nps

A literature plot showing surface area against LB trough area for nanoparticle species (platinum-cobalt) is given in Figure 3.11. A typical profile recorded on the LB trough (referred to as an isotherm) for platinum/PVP nps is shown in Figure 3.12.

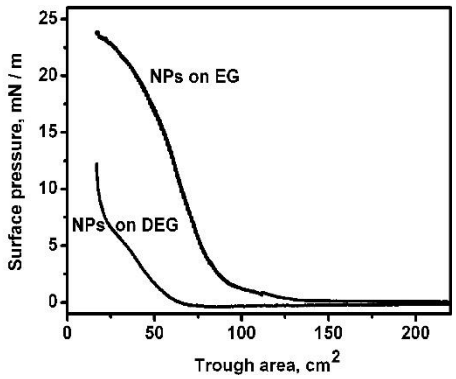

Figure 3.11. Literature plot of surface area against LB trough area for the deposition of cobalt-platinum nanoparticles on two differing supports (denoted by EG and DEG). Reprinted with permission from (Benkovičová, M.; Végsö, K.; Šiffalovič, P.; Jergel, M.; Majková, E.; Luby, Š.; Šatka, A. Preparation of Sterically Stabilized Gold Nps for Plasmonic Applications. Chem. Pap. 2013, 67 (9)). Copyright (2013) American Chemical Society.

For Figure 3.12 any surface pressure below the plateau seen at 40 mN m^{-1} (which was associated with multilayer formation) would be expected to give a monolayer particle coverage. A value close to the plateau was chosen in order to give a tightly packed particle distribution. Correspondingly the clean hemisphere was dip coated by removal from the trough in the vertical direction once the platinum/PVP np surface had reached a surface pressure of 30 mN m^{-1}. A uniform monolayer surface, of platinum nanoparticles, was expected to form. In agreement the work of Zhang *et al.,*[29] for rhodium nanoparticles also capped with polyvinylpyrrolidone, showed that in order to receive a surface coverage of 0.8 *(i.e.* a densely packed surface) a surface pressure of 25 mN m^{-1} was required for dipping of the sample.

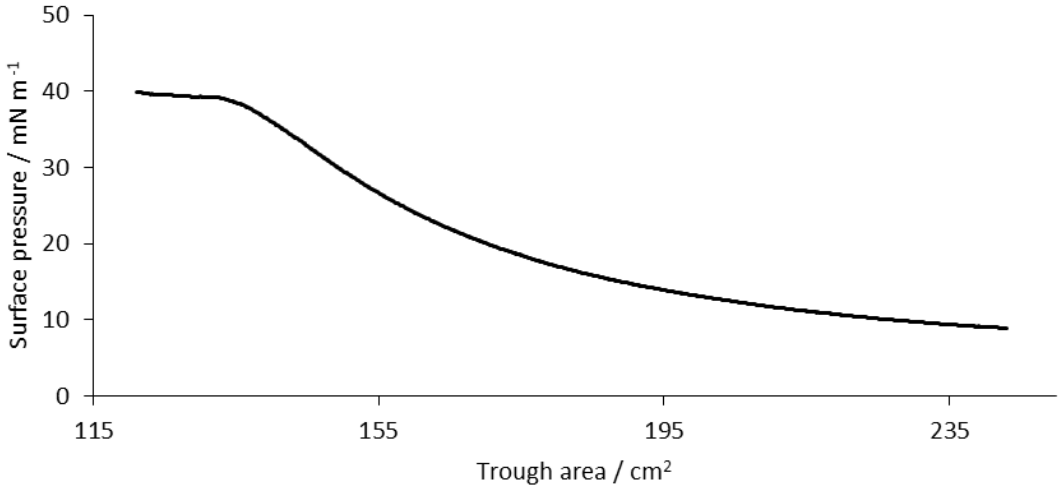

Figure 3.12. Isotherm showing surface pressure versus LB trough area for a typical deposition of platinum/PVP nps.

Several batches of platinum/PVP nps were studied (Figure 3.13) by the method given above, to ensure tightly packed monolayer distributions were consistently achieved, as determined by the repeatability of the isotherm shape.

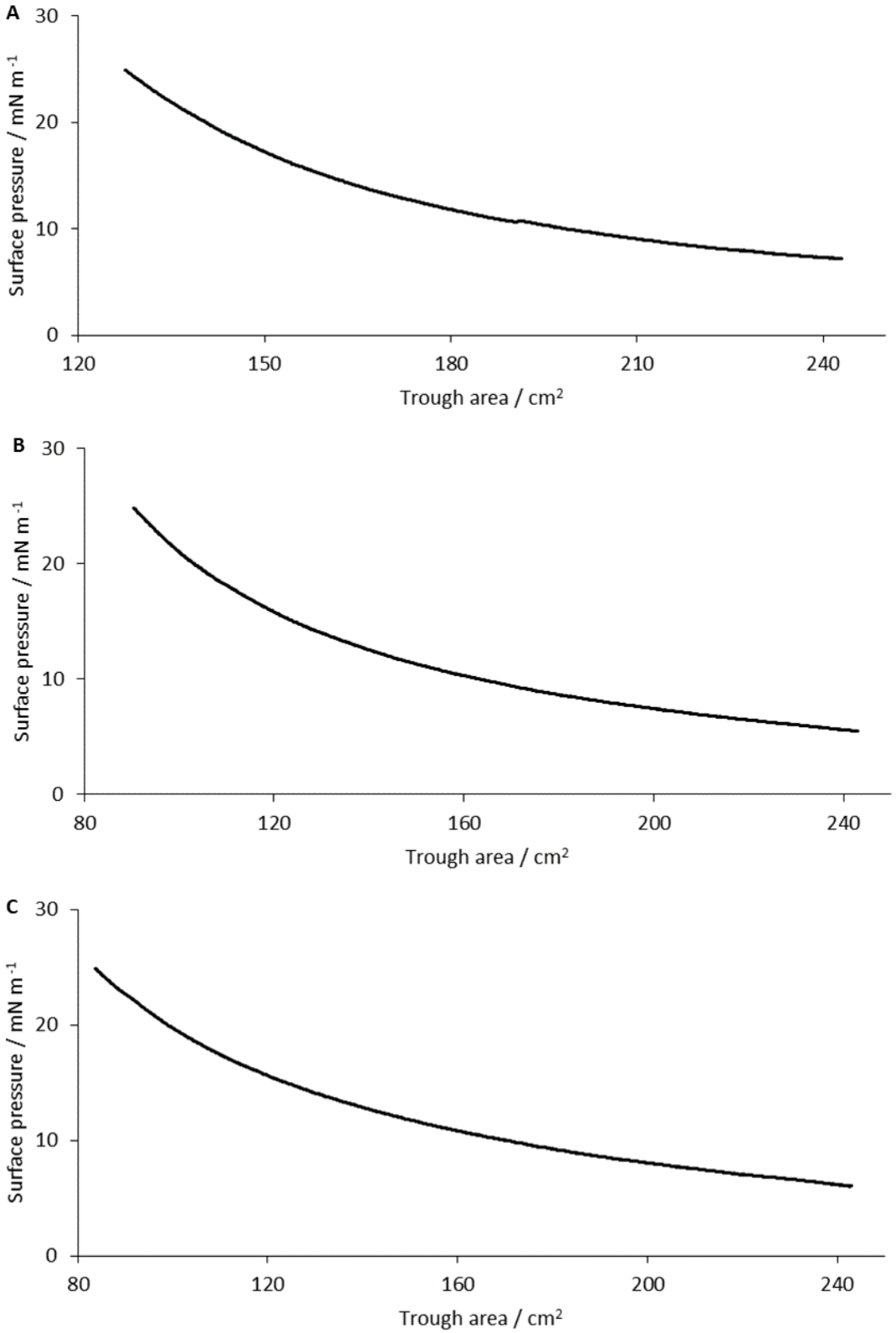

Figure 3.13. Isotherm showing repeatable results for surface pressure versus LB trough area for three differing depositions of platinum/PVP nps.

Initially nanoparticles were stored in chloroform prior to deposition. Chloroform was chosen as a highly volatile solvent was required to allow fast evaporation of the solvent on the surface of the LB trough. However, it was quickly found that for samples stored for any significant period in chloroform, evaporation of the solvent lead to agglomeration of the nanoparticles. For such samples compression of the barriers on the LB trough (which decreased the trough surface area) did not give lead to the expected gradual increase in the surface pressure. Accordingly, the experimental procedure was modified with samples being stored in ethanol and only transferred to chloroform on the day of use. This solvent exchange was performed using an anti-solvent precipitation method, as is typically used for washing the particles during purification. The samples were also vigorously sonicated, in both solvent systems to prevent any particle agglomeration. Upon implementing this revised procedure reproducible isotherms were obtained, and no evidence of suspected particle agglomeration (as would be indicated by the absence of a pressure rise) was seen.

Overall the isotherm data presented suggested that reproducible, uniform surfaces were formed for platinum/PVP using LB deposition methods. Such surfaces should be suitable for study by TIR Raman.

3.2.1.1. TEM imaging of platinum/PVP nps deposited onto a TEM grid via LB trough methods

TEM analysis was recorded for platinum/PVP np samples where the TEM grid was prepared using both a standard (Section 3.1.1 Figure 3.1) and an LB trough deposition technique (Figure 3.14). TEM of nanoparticles taken directly from the LB trough was recorded as a method of assessing the quality of LB deposited films. This was done by dropping a TEM grid on top of the trough and picking it up again using tweezers.

Particle appearance and size was similar to those deposited *via* the standard method. Particle coalescence appeared a little more severe, although it is hard to tell if this is a result of the drying behaviour, of the more compressed film, once on the TEM grid. The particle size centred to a slightly smaller value (3 ± 1 nm *vs.* 4 ± 1 nm), than for the standard drop casting method. The reason for this is unclear, but the difference is only small. Overall TEM imaging in this manner, which reproduces the surface of the LB trough on the TEM grid, gave a good indication of formation of the desired tightly packed particle film without significant changes in the properties of the as prepared nanoparticles examined by TEM from the bulk solution by the standard drop casting method.

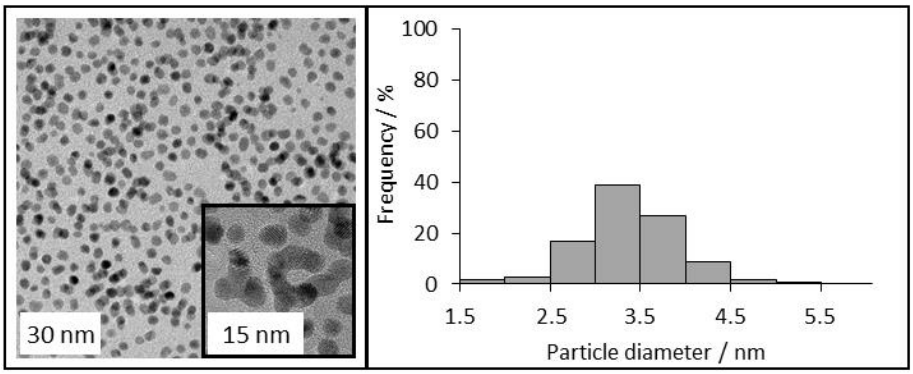

Figure 3.14. (left) Typical TEM image of as for synthesised platinum/PVP nps deposited onto the TEM grid using the LB deposition method (prepared as outlined in Section 2.2.1.1, and deposited as described in Section 2.2.5.9), (right) corresponding particle size distribution (3 ± 1 nm) obtained from multiple images of this sample.

3.2.1.2. XPS investigation of platinum/PVP nps LB deposited onto substrates

XPS analysis was conducted for platinum/PVP nps. The goal of this was to quantify the coverage of platinum particles on the substrate. XPS is a surface sensitive technique, and as such should allow deduction of the metal loading for the LB deposited platinum films. By use of a flood gun, XPS can be carried out with non-conducting substrates (unlike SEM, where conducting samples are required), and can be used to quantify loading over a large area. This is crucial in this project as it allows direct comparison of the deposition on the native oxide surface of a silicon wafer,[30] as used for SEM, to a bulk silica glass, such as the silica hemisphere optic used in TIR Raman.

XPS was recorded for LB deposited samples dipped once and twice on a silicon wafer. This was expected to give monolayer and multilayer coverage. Material dipped once onto a silica window was also prepared. Three regions of the silicon wafer were sampled, and ten for the silica window. A typical spectrum is shown in Figure 3.15. All other spectra recorded are given within the Appendix, Figures 3A.4-3A.18.

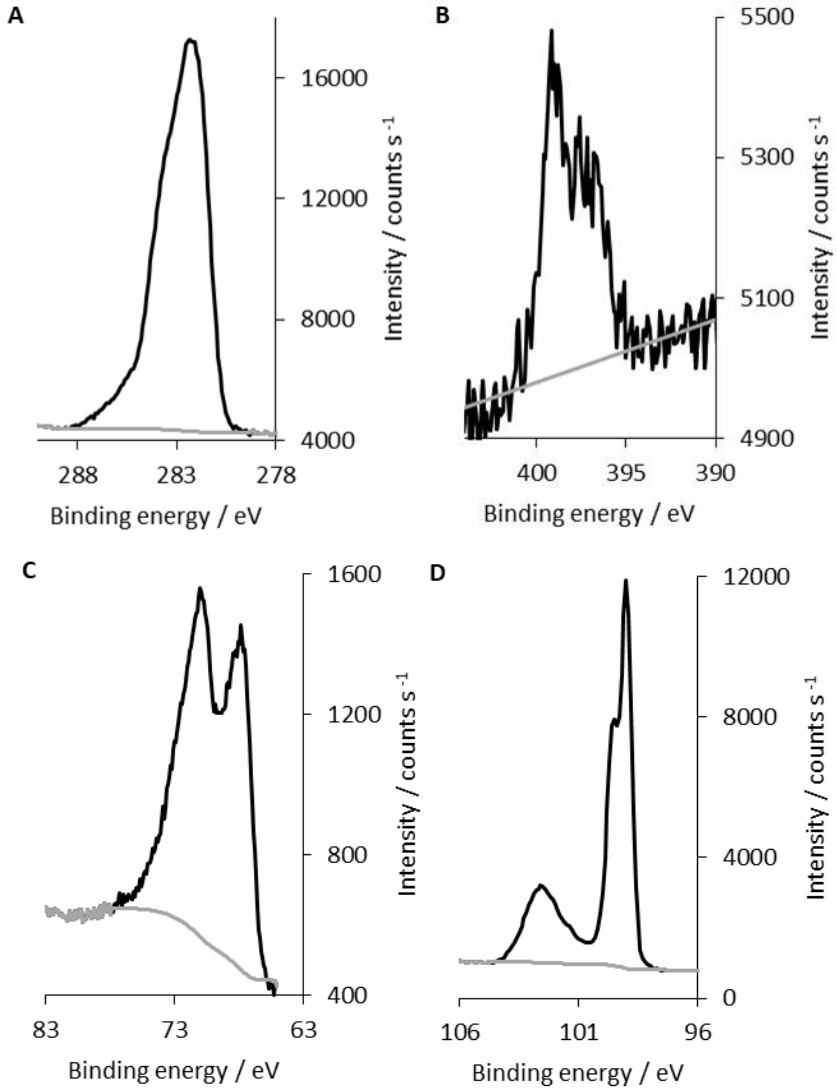

Figure 3.15. XP spectra for sample one of three for platinum/PVP nps supported upon a silicon wafer deposited using, LB techniques with one dipping, for the following binding energy regions: A) carbon 1s, B) nitrogen 1s, C) platinum 4f, and D) silicon 2p. Spectra is shown in black and the Shirley background fitted is given in grey, with the exception of spectra B where a linear background was fitted.

XPS integral ratios were obtained by careful selection of the region of interest, applying a Shirley background (with the exception of spectra B in Figure 3.15 where a linear background was fitted) and integrating the Pt 4f and Si 2p regions using Casa XPS software and the in-built function which takes into account the relative sensitivity of the different elements. An analyser function of 1 over all regions studied is assumed based on information from the service provider. From this data the atomic ratio of carbon/nitrogen and platinum/silicon was calculated, values can be found in Table 3.3 below. For a vinylpyrrolidone monomer unit an atomic ratio of carbon/nitrogen of 6/1 would be expected. Although some of the values for the silica window are within this range (around 12:1) the majority of values recorded have

a significantly higher carbon content, perhaps to adventitious carbon resulting from aerial contamination.

Table 3.3. Tables to show atomic% (At.%) ratios of carbon/nitrogen (C/N), and platinum/silicon (Pt/Si) calculated from fitting of spectra using Casa XPS (Section 2.2.5.5), for three platinum/PVP LB deposited samples- two silicon wafer deposited sample with one and two layers- five data points, and silica window (single layer LB deposited) – ten data points.

1 layer silicon wafer	C/N ratio At.%	Pt/Si ratio At.%
1	47.5/1.0	1.0/49.3
2	49.3/1.0	1.0/8.0
3	58.9/1.0	1.0/21.0

2 layer silicon wafer	C/N ratio At.%	Pt/Si ratio At.%
1	22.7/1.0	1.0/3.2
2	18.7/1.0	1.0/2.1
3	21.1/1.0	1.0/2.1

Silica window	C/N ratio At.%	Pt/Si ratio At.%
1	64.1/1.0	1.0/3.7
2	15.0/1.0	1.0/1.9
3	86.7/1.0	1.0/2.9
4	31.5/1.0	1.0/1.8
5	137.9/1.0	1.0/6.3
6	12.9/1.0	1.0/1.3
7	95.2/1.0	1.0/3.6
8	99.0/1.0	1.0/3.5
9	27.3/1.0	1.0/1.7
10	14.5/1.0	1.0/1.6

These values were then converted into a percentage coverage of the surface using the following equation;

$$Pt\ fractional\ coverage = \frac{Pt\ area}{Pt\ area + Si\ area} = \frac{1}{1 + \text{atomic ratio}\ \frac{Si}{Pt}} \qquad \textit{Equation 3.1}$$

In order to find the factional coverage of platinum (Pt) using Equation 3.1, it was assumed that the surface was either bare silica or had a depth of platinum equivalent to one particle, and that XP spectra therefore sees either all platinum or all silicon. The ratios of these two areas were then calculated, based on the escape depth of the electrons detected during the XPS measurement given below:

$$P(d) = exp\ (\frac{-d}{\lambda})$$

For a probability of an electron escaping P(d), at a depth of the electron d, with a inelastic mean free path of the element λ (1.5 nm for platinum, and 3.1 nm for silicon).

To simplify this, it was assumed that particles (which were roughly spherical) could be treated as cubes of equal volume using the geometric relation:

$$d_s = 2 \times \sqrt[3]{\frac{l^3}{\frac{4}{3}\pi}}$$

where d_s is the diameter of a sphere and *l* is the edge length of a cube of corresponding volume. The final coverage was calculated by interconverting back to spheres to obtain the area. The values of surface coverage were calculated by this method and are given in Table 3.4. Full values used in the calculations can be found in the Appendix, Table 3A.1.

As can be seen from Table 3.4 for the silicon wafer irreproducible results were obtained with a single dip, but produced an average of ~11%. More consistent results were obtained by dipping the sample twice of around 50%. The reason for this is unclear, and further data may help understand if the single dip samples were erroneous. The value of 50% obtained for 2 layers is double that typically seen for a single layer coating using SEM (Section 3.6.1.1).

For the silica window platinum coverage values between 26 to 69% were seen with an average of 50% (and a standard deviation in the sample points of 14%). Because the goal of using XPS was primarily to probe the non-conducting silica sample that could not be examined by other means, 10 different regions were examined to build up a statistically valid average and this suggested the overall coverage was 50 ± 5%.

Although the XPS data from the silica glass was slightly more variable than that from the silicon wafer, it has the merit of showing the same approximate coverage can be expected for coating the optics. Inhomogeneity at different points on glass can speculatively be ascribed to the relative surface flatness of the two substrates. The silica wafer forming into

almost atomically flat layers versus glass which is polished and so still may have a less uniform surface area at different points on the sample.

Table 3.4. Tables to show platinum (Pt) coverage, calculated from fitting of spectra using Casa XPS (Section 2.2.5.5), for three platinum/PVP LB deposited samples- two silicon wafer deposited samples with one and two LB deposited layers respectively with five data points surveyed and a silica window (single layer LB deposited) with ten data points surveyed.

1 layer silicon wafer	Pt coverage as spherical particle / %
1	4
2	21
3	9

2 layer silicon wafer	Pt coverage as spherical particle / %
1	42
2	54
3	55

Silica window	Pt coverage as spherical particle / %
1	38
2	57
3	44
4	60
5	26
6	69
7	39
8	39
9	61
10	62

3.2.1.3. SEM investigation of platinum/PVP nps method LB deposited onto substrates

SEM imaging took place for freshly deposited platinum/PVP nps deposited on a silicon wafer. This would allow for exploration of the surface morphology of the deposited material including the presence of any agglomerates. Due to the high carbon content of the capping

agent it was not possible to image the sample without first applying a protective coating. To this end a chromium coating was applied as conducted by colleagues in physics. Imaging for the chromium coated sample is given (Figure 3.16 A) and shows a thin film with no evidence of agglomeration, but individual particles are difficult to see. Plasma cleaning of the sample for a short time, in this case 10 s, allowed for the resolution of individual particles (Figure 3.16 B). For these small particles we detect a single film. It should be noted that a longer plasma cleaning time is required for full removal of the capping agent for study *via* Raman spectroscopy (as shown in Section 3.6.1.1). These results are indicative of formation of the desired thin film of nanoparticles upon the silicon wafer, with no evidence provided for any agglomeration in the sample.

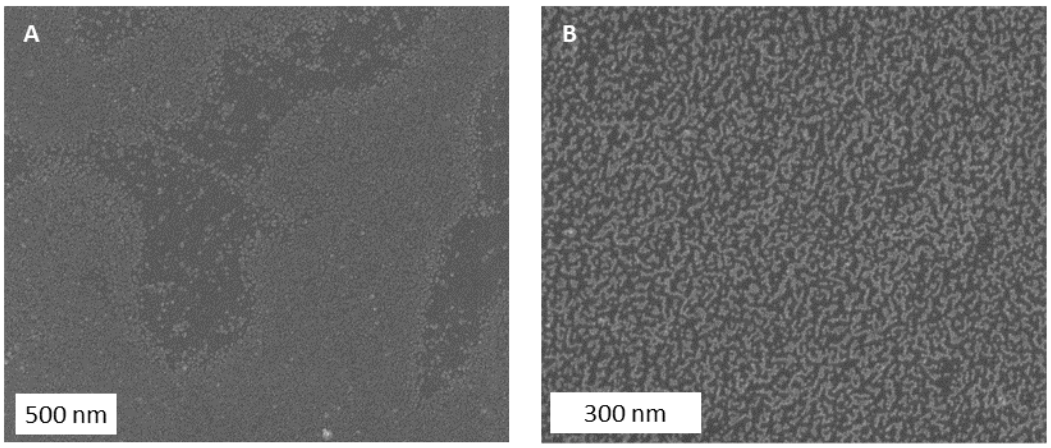

Figure 3.16. *SEM images for platinum/PVP nps deposited using LB deposition (1 layer) on a silicon wafer, with a chromium coating added to facilitate imaging. Samples were then treated as follows: A) no treatment, B) plasma cleaned for 10 s to allow for the resolution of individual particles.*

3.2.2. Silver/OAm/OAc nps

In the case of silver nanoparticles the capping agents (oleylamine and oleic acid) are hydrophobic. When the silver nanoparticles were placed on the water surface of the LB trough, the surface pressure was initially seen to drop as the solvent (chloroform) evaporated. The decrease in surface pressure can be explained by the solvent evaporating to leave the hydrophobic silver nanoparticles, which are no longer held rigid by the hydrophobic solvent within the layer structure.

The first attempt of monitoring surface pressure for decreasing trough area with silver nanoparticles (given in the Appendix Figure 3A.3), gave a gradient which did not reach a plateau, indicating multilayer formation had not been reached. Further material was therefore added to the trough surface at the start of the experiment in order to increase the

starting surface pressure. Figure 3.17 shows the surface pressure versus trough area isotherm recorded for this increased starting pressure.

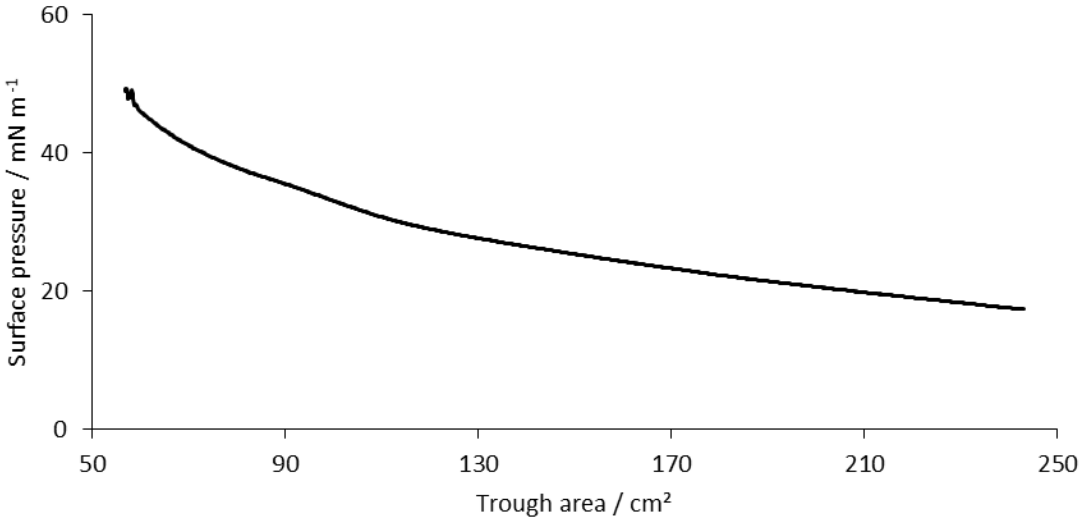

Figure 3.17. Isotherm experiment recorded for silver/OAm/OAc nps showing surface pressure against area of trough, with high starting surface pressure.

It should be noted that dropwise addition of nanoparticles to the water surface of the LB trough was stopped when it appeared fully saturated, in that further drops placed on the surface would not disperse and formed a droplet sat on the surface. In Figure 3.17, it can be seen that the plateau region of the graph was still not reached. However, since the surface was fully saturated a higher surface pressure could not have been reached using our trough. The curve seen was smooth across all trough areas and the gradient increased towards higher surface pressures as the nanoparticles moved closer to adopting a multilayer. From this curve it might be expected that deposition of silver nanoparticles on the hemisphere should give a tightly packed monolayer surface when particles have been compressed to give a surface pressure of ~40 mN m^{-1}. This is a higher surface pressure than required for platinum/PVP nps, but is clearly still below the point multilayers are formed. The silver nanoparticles are capped with oleylamine, these long chain amines provided steric hindrance at some distance, but could gradually be compressed or forced out of the surface, with the silver nanoparticle still remaining in a 2-D layer. This may provide a reason for the silver nanoparticles reaching higher surface pressures.

3.2.2.1. TEM silver/OAm/OAc nps deposited via standard and LB trough methods

TEM samples for the silver nanoparticles were prepared using the LB trough deposition technique as before in order to give an indication of the coverage on the surface by LB deposition on the hemisphere. Based on the agreement between XPS, SEM and TEM analysis

for the platinum/PVP nps it was anticipated TEM imaging would provide a good method to monitor the success of the LB deposition process.

TEM images of the LB deposited sample are shown in Figure 3.18 and can be compared to the standard drop cast method in Section 3.1.2.1 (Figure 3.2). Both images show a majority of small spherical particles along with some larger particles. The particle distribution appeared to broaden slightly for the LB trough deposited sample, but is similar to that expected from the starting nanoparticles. Comparison to the polyvinylpyrrolidone capped nanoparticles also prepared by LB deposition onto the TEM grid, (Section 3.2.1.1 Figure 3.14), revealed a slightly higher surface packing of particles for the amine and acid capped particles. This was anticipated due to the relative size of the two capping agents. With the less bulky amine/acid groups allowing closer proximity of the neighbouring nanoparticles than the polymer and so resulting in a more tightly packed surface.

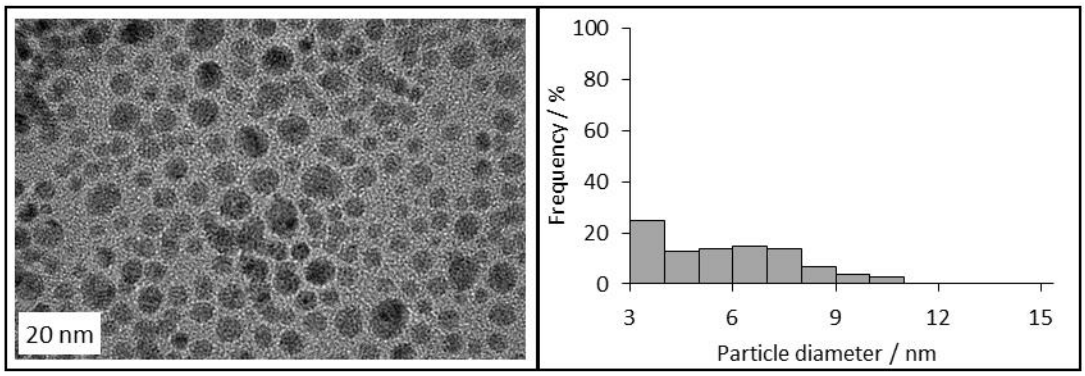

Figure 3.18. (left) Typical TEM image of as synthesised silver/OAm/OAc nps with a 1 h ripening time, deposited onto the TEM grid using the LB deposition method (prepared as outlined in Section 2.2.1.4, and deposited as described in Section 2.2.5.9), (right) corresponding particle size distribution (6 ± 2 nm) obtained from multiple images of this sample.

3.3. Confocal Raman studies of platinum/PVP nps

Platinum/PVP nps, deposited onto a silicon wafer *via* LB techniques, were studied *via* confocal Raman spectroscopy. Confocal Raman spectroscopy was undertaken in order to provide a reference using bulk samples and also investigate whether it would be sensitive to the monolayer samples. Spectroscopy took place at laser powers lower than those that caused sample damage. It was anticipated that sensitivity would be low as this is a key potential advantage of TIR Raman spectroscopy.

All confocal Raman spectra were obtained, using the conditions detailed within sections 2.2.4.1, and 2.2.4.1.1. A 532 nm laser excitation wavelength was used for all confocal Raman

spectroscopy. In order to use a setup that could also be used for TIR Raman spectroscopy the beam was delivered through a separate lens to a focal point on the sample co-incident with the focal point of the objective (in contrast to most Raman systems where the objective is used to deliver and collect the light). An incident beam angle of 73° was used for all of the spectra shown below, which are for samples deposited upon a silicon wafer. Glass substrates had been trialled (at a lower 55° incident angle) but only fluorescence had been seen. Raman spectra were first recorded for a clean silicon wafer (Figure 3.19 A) to allow for backgrounding of any subsequent spectra. Initially, monolayer samples of platinum/PVP nps (deposited using LB techniques) were studied (Figure 3.19 B). Initially, this spectrum was recorded at a laser power of 1.5 mW at the sample, as determined by a laser power meter. Under these conditions no Raman bands were detected (including those attributed to the silicon wafer). Correspondingly the laser power was increased to 15 mW (this power again being measured at the sample using a laser power meter). Optical microscopy did not indicate any degradation had taken place for the sample under the laser beam at this increased laser power, although it is likely that monolayer films would be too thin for this to be seen *via* optical microscopy. Under these conditions bands assigned to the silicon wafer were seen, however, no further bands attributed to the capping agent were detected above the silicon background. Significant fluorescence was seen in this spectrum and was seen to increase in intensity towards higher wavelengths. Drop cast platinum/PVP np samples were subsequently studied. These samples were prepared by depositing a drop of the nanoparticle solution onto the surface of a silicon wafer using a glass pipette. This allowed for a thicker layer of nanoparticles to be deposited, which might give an increased likelihood of detecting the organic capping agent, however increased levels of fluorescence might also be expected. For the drop cast sample (Figure 3.20 A) initial spectra were taken with a laser power at the sample of 15 mW (again measured using a laser power meter). Under these conditions sample degradation was seen to take place. This was seen as a blackened region using optical microscopy, to examine the drop cast samples after laser exposure. Correspondingly the laser power at the sample was reduced to 11.7 mW. This lead to a reduction in the number of Raman scattered photons, and so to a reduction in the signal intensity. At this reduced power no laser induced sample damage was seen. However, a very significant fluorescent background was seen which again increased with intensity towards higher wavelengths. Fluorescence (being much stronger than Raman) is likely to obscure the weaker Raman peaks we hope to detect. The laser induced sample damage seen may have been related to the high levels of fluorescence observed. In order to fluoresce, the sample absorbs large

quantities of light and emits at lower frequency, potentially causing a significant heating effect. It is thought this heating effect may be causing sintering and agglomeration of the nanoparticles and/or damage to the carbon containing polymer (polyvinylpyrrolidone) used as capping agent. Coupling the severe fluorescence seen with the reduced laser powers which could be used, the likelihood of resolving Raman bands for the capping agent was low. Indeed only when the capping agent (polyvinylpyrrolidone) alone was measured as a bulk sample deposited on a silicon wafer (as shown in Figure 3.20 B) was it possible to see any Raman bands (except from the silicon) in addition to the fluorescence. These bands were assigned as given in Table 3.5 and good agreement with the literature was seen.[31] However, as noted a significant fluorescent background was also observed.

In summary, for platinum/PVP nps confocal Raman spectroscopy did not allow for the detection of the capping agent species on the nanoparticles, and low sample damage thresholds were observed using simple optical spectroscopy. For a higher concentration of the capping agent alone Raman bands expected from the literature could be detected and assigned, but even then a significant fluorescent background was seen. The fact that Raman bands were not seen for the drop cast particle solution but were for bulk polyvinylpyrrolidone suggests that the fluorescence is made worse as a result of either the presence of the nanoparticles or the changes to the polyvinylpyrrolidone and other entrained species as a result of the particle synthesis process. In order to overcome the fluorescence seen a series of attempted purification processes were undertaken and these are described in the next section.

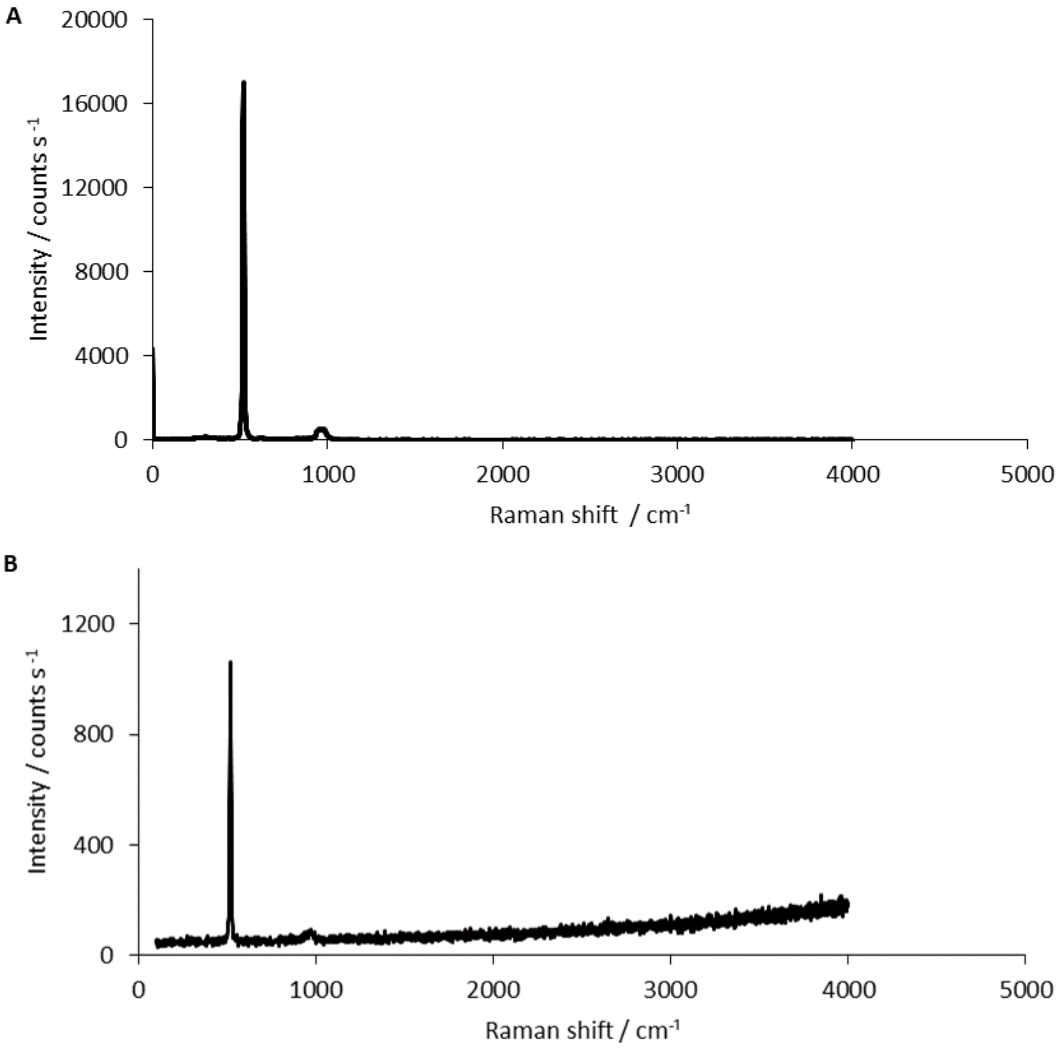

Figure 3.19. Selected Raman spectra from confocal Raman spectroscopy recorded at an incident beam angle of 73°, recorded on System 1 under the standard conditions described in Section 2.2.4.1.

A) clean silicon wafer, recorded for use as background. Spectrum recorded for 4 lots of 10 s acquisitions, at a laser power of 20 mW as measured at the sample using a laser power meter.

B) monolayer of platinum/PVP nps on silicon wafer. Spectrum recorded for 4 lots of 30 s acquisitions, at a laser power of 15 mW as measured at the sample using a laser power meter.

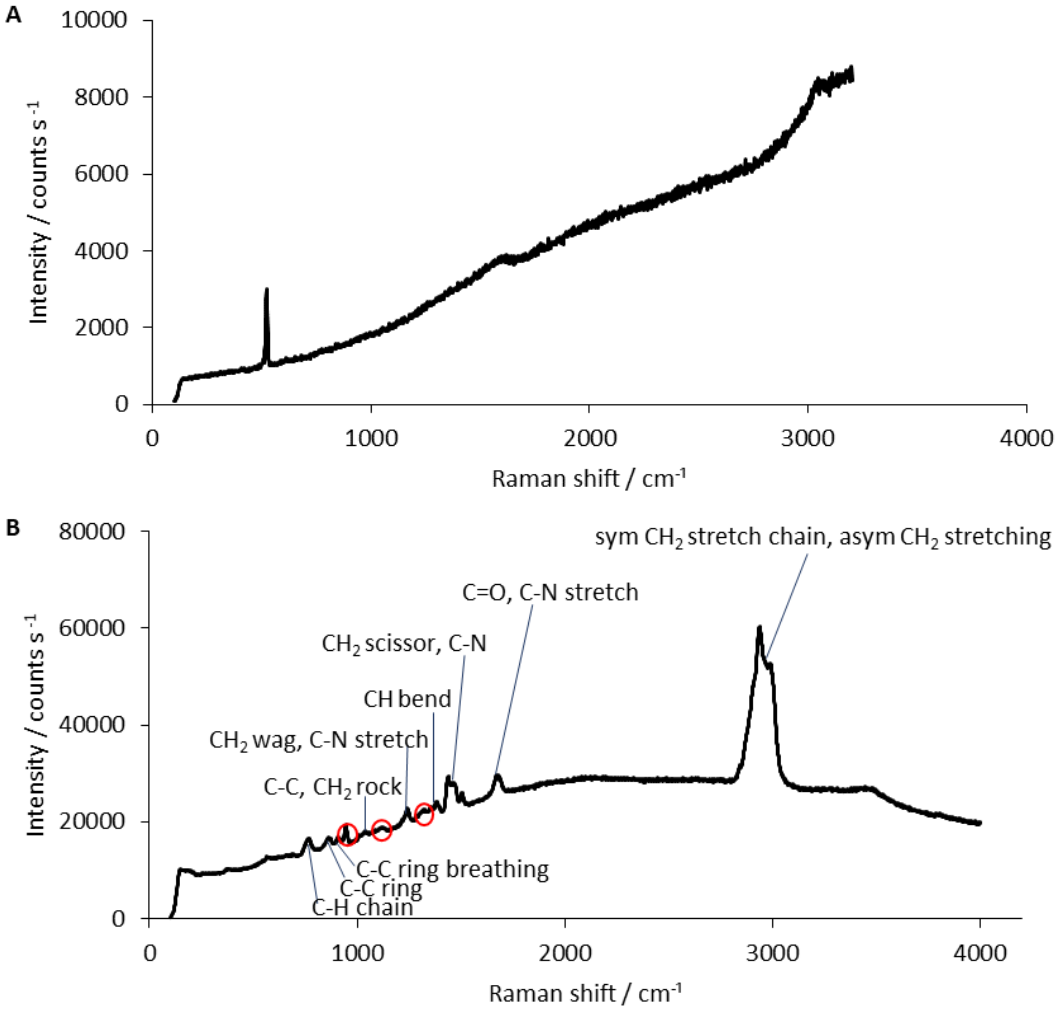

Figure 3.20 Selected Raman spectra from confocal Raman spectroscopy recorded at an incident beam angle of 73°, recorded on System 1 under the standard conditions described in Section 2.2.4.1. Where sym=symmetrical vibration, and asym=asymmetrical vibration.

A) drop cast platinum/PVP nps on silicon wafer. Spectrum recorded for 4 lots of a 30 s acquisitions, at a laser power of 11.7 mW as measured at the sample using a laser power meter.

B) polyvinylpyrrolidone powder on a silicon wafer. Spectrum recorded for 4 lots of 10 s acquisitions, at a laser power of 20 mW as measured at the sample using a laser power meter. Bands marked by a red circle were unassigned.

Table 3.5. Assignment of Raman stretches for polyvinylpyrrolidone on a silicon wafer from confocal Raman spectroscopy. Assignments made from Borodko et al..[31] *Where str=stretch, wagg=wagg vibration, and asym=asymmetrical vibration.*

Assignment	**Raman shift / cm^{-1}**
C-H chain	774
C-C ring	864
C-C ring breathing	936
C-C, CH_2 rock	1042
CH_2 wagg, C-N str	1245
CH bend	1335
CH_2 scissor, C-N	1450, 1511-shoulder
C=O, C-N str	1671
Sym CH_2 str chain, asym CH_2 str	2939, 2994-shoulder
unassigned	948, 1111, 1427

3.4. Polyvinylpyrrolidone characterisation and purification

As discussed in Section 1.5.1.3.1, the capping agent is important in nanoparticle synthesis, due to its role in stabilising the metal nanoparticle. However, the composition and purity of the capping agent species, is a subject which is often overlooked. Polyvinylpyrrolidone capped nanoparticles had shown significant fluorescent background, when studied *via* confocal Raman spectroscopy (Section 3.3). Capping agent impurities, could be a possible source of the fluorescent background observed. The packing of the nanoparticles, is of importance in this study, due to the desire to make monolayer particle films for study *via* TIR Raman spectroscopy. For polymer species, such as polyvinylpyrrolidone, it is plausible that the ability of the molecule to act as a capping agent or particle packing, could be impacted by the number of monomer repeat units. The M_w of the polymer is known to effect the size of the nanoparticle.[32]

Characterisation of polyvinylpyrrolidone was conducted, in order to gain insight into the materials intrinsic properties as well as possible sources of the observed fluorescence.

3.4.1. ^{13}C and ^{1}H nuclear magnetic resonance (NMR) spectroscopy

^{13}C and ^{1}H NMR spectroscopy were recorded for polyvinylpyrrolidone (as purchased from Sigma Aldrich) to assess the polymer composition, as well as the presence of any impurities. For ^{13}C NMR spectra all of the carbons were assigned as expected, and in accordance with

Dutta *et al.*.[33] δC(400 MHz; $CDCl_3$, Me_4Si) 176 ppm (1 C, s, **1-CO**), 44 (1 C, s, **4-CH_2**), 42 (1 C, s, **5-CH**), 31 (1 C, s, **2-CH_2**), 30 ppm (1 C,s, **6-CH_2**), and 18 (1 C, s, **3-CH_2**). The numbers given in bold along with the differing carbon substituents correspond to those given in the Appendix in Figure 3A.19 A. For spectra taken both before and after purification the shape of the peak centred around 175 ppm, assigned to 1-CO, appeared to contain some fine structure suggesting the possible presence of different conformations;[34] the spectra after such purification is shown in the Appendix in Figure 3A.19 A.

^{1}H NMR spectra was assigned and was in accordance with Dutta *et al.*.[33] δH(400 MHz; $CDCl_3$, Me_4Si) 3.9-3.4 ppm (1 H,s, s, **2**), 3.4-3.0 (2 H, s,s **5**), 2.6-2.2 (2 H, m,s **3**), 2.1-1.6 (2 H, s,s **4**), and 1.9-1.3 (2 H, m, **1**). The numbers or substituent given in bold at the end of the bracket correspond to those given in the Appendix in Figure 3A.19 B. There is an unassigned peak seen at 2.9 ppm which was not seen in the literature spectra. This peak could have been due to an impurity, and was not accounted for by any expected solvent peaks. Otherwise good spectral agreement was seen.

Both NMR spectra, gave relatively good agreement and indicated a low number of NMR active impurities were present. There was no significant evidence from NMR spectroscopy that impurity, or composition issues were likely to contribute to the Raman fluorescence seen. Polyvinylpyrrolidone is thought to be made commercially by free radical polymerization,[35] but if the particular controlled chain length version purchased was prepared using metal salts these could be undetectable impurities by NMR that could still fluoresce.

3.4.2. UV-visible (UV-vis) spectroscopy

UV-vis spectroscopy was used to indicate if the observed fluorescence might be wavelength dependent. In UV-vis spectroscopy photons cause excitation to higher energy states. Relaxation can then take place by fluorescence, non-radiative relaxation, or a mixture of the two. Hence, although there is no guarantee that if UV-vis absorbance is detected fluorescence has occurred, it is one possibility, and if no absorbance is seen no fluorescence occurs. UV-vis spectroscopy can therefore be a viable method of determining at what wavelengths fluorescence might occur. UV-vis spectra obtained for polyvinylpyrrolidone and platinum/PVP nps are shown in Figure 3.21. It should be noted that all spectra were recorded at a concentration of 1 mg mL^{-1} in ethanol. For platinum/PVP nps, based upon the synthesis, the upper bound for the concentration of polyvinylpyrrolidone in ethanol was calculated to be 0.92 mg mL^{-1} if none was removed during washing of the nanoparticle (the nanoparticle

was washed a total of 8 times as detailed in Section 2.2.1.1). So the value was suitably close to the concentrations used for polyvinylpyrrolidone and vinylpyrrolidone standards without the nanoparticles. Full details of this calculation can be found within the Appendix. It can be seen that platinum/PVP nps did absorb strongly at 530 nm, however at higher wavelengths this absorbance was significantly reduced. This suggested that increasing the laser excitation wavelength should reduce absorbance, and so possibly also fluorescence and this will be discussed in the design of a new laser system in Chapter 5. This result also suggests the polyvinylpyrrolidone is less likely to fluoresce in the absence of platinum nanoparticles, as indeed was observed in the confocal Raman experiments. The absorbance profile of the platinum/PVP np increasing quasi-exponentially from the visible down into the UV (decreasing wavelength) has been seen previously to be in very loose qualitative agreement with Mie scattering theory, but with a strong dependence on shape and/or size.[36] Mie theory predicts the scattering cross section of particles much smaller than the wavelength of light to be weak compared to their absorption.[37,38] However only loose qualitative agreement with the theory was seen, and the fact that the fate of the energy absorbed is unknown lead to the conclusion that the polyvinylpyrrolidone could increase the ratio of radiative (fluorescent) versus non-radiative decay. For polyvinylpyrrolidone alone no absorption was seen at 530 or 660 nm (the laser lines considered in this work have been 532 and 660 nm), but at lower wavelengths a strong absorbance is seen (presumably $\pi - \pi^*$ transitions of the carbonyl), and this could potentially stimulate higher levels of fluorescence so this region of excitation should be avoided.

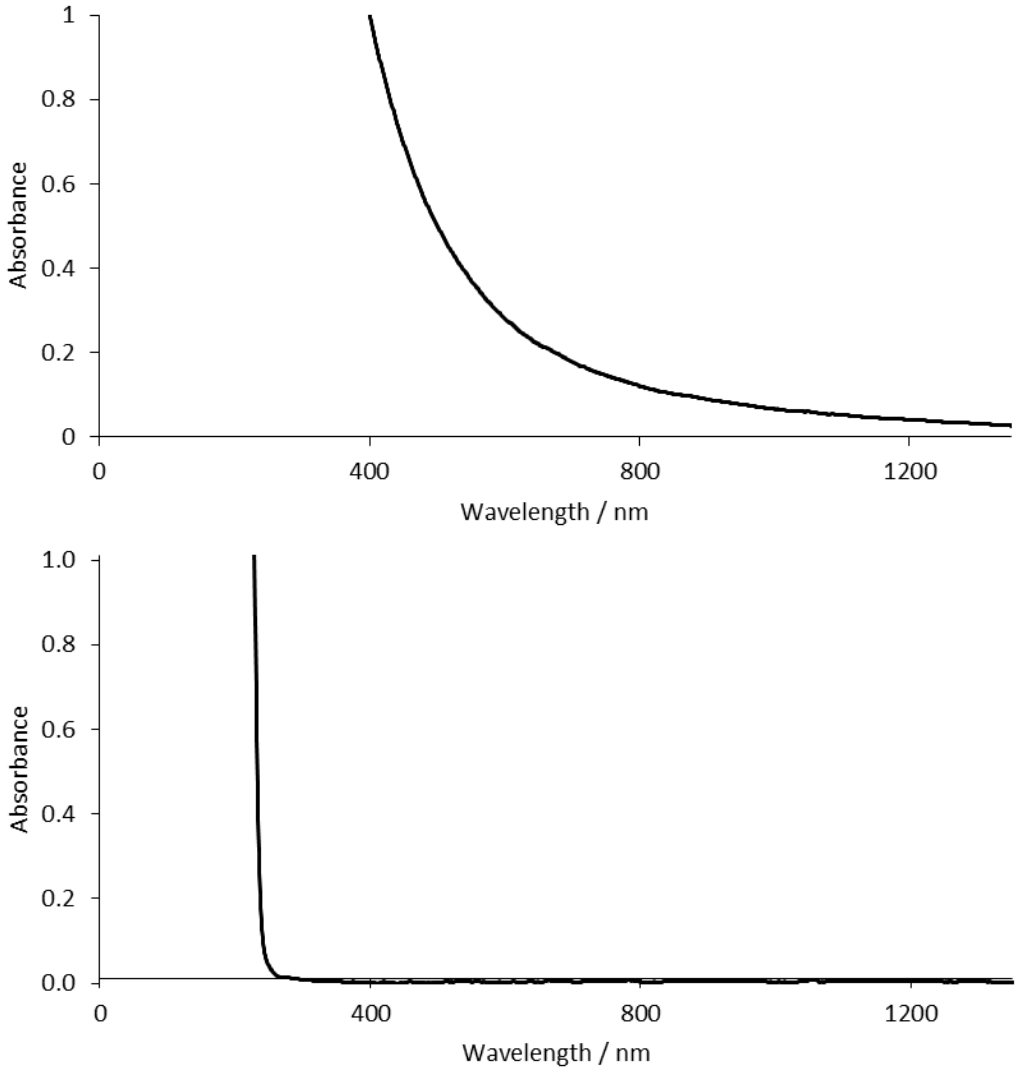

Figure 3.21. UV-vis spectra for, top platinum/PVP nps (synthesised according to Section 2.2.1.1 and washed a total of 8 times,) and bottom polyvinylpyrrolidone with both at a concentration of 1 mg mL^{-1} in ethanol. Spectra are shown up to 1350 nm due to the detection limit of the instrument.

The UV-vis spectra of the monomer unit vinylpyrrolidone was also recorded (Figure 3.22) to establish if a difference existed between the fluorescence of the monomer and polymer. If so then the polymerisation process used might contribute to the fluorescence seen for platinum/PVP nps (*e.g*. due to metal impurities from a polymerization catalyst as suggested previously). The spectrum showed minimal absorbance in the range of 530 and 600 nm. However, a small absorbance just below 500 nm was observed. There did not appear to be any significant increase in absorbance from the monomer compared to the polymer species.

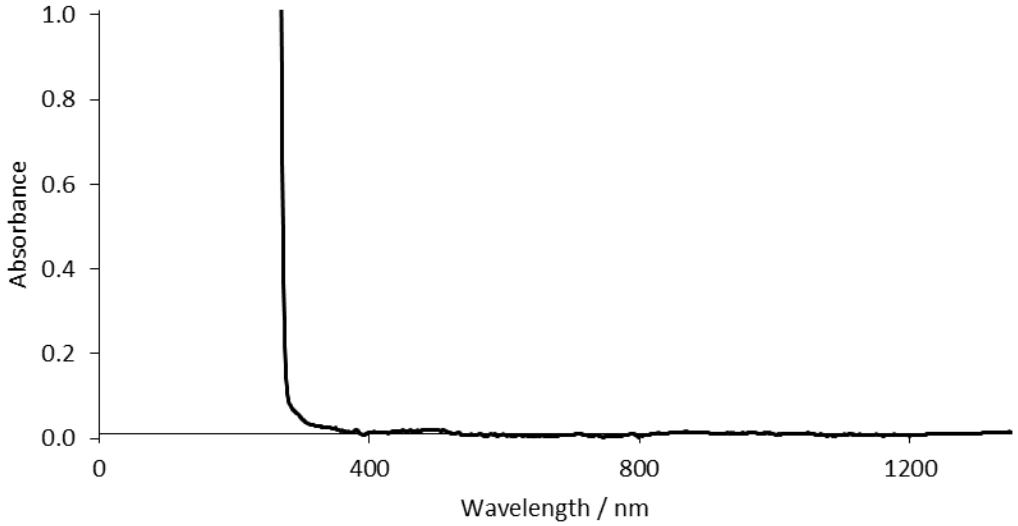

Figure 3.22. UV-vis spectra for vinylpyrrolidone as purchased from Sigma Aldrich. Spectra are shown up to 1350 nm due to the detection limit of the instrument.

As synthesised nanoparticles were washed, using a solvent and anti-solvent method (see Section 2.2.1.1). This allowed for the removal of excess reagents such as capping agent or reducing agent for the as formed nanoparticles. The effect of washing for platinum/PVP nps was also explored using UV-vis spectroscopy. The UV-vis spectra for an unwashed sample is given in Figure 3.23. As anticipated higher levels of absorbance were seen for the unwashed sample. This may be attributed to the presence of impurities or just a greater quantity of polyvinylpyrrolidone, either of which may contribute to the observed fluorescence. Hence this verifies the importance of thorough washing of the nanoparticles.

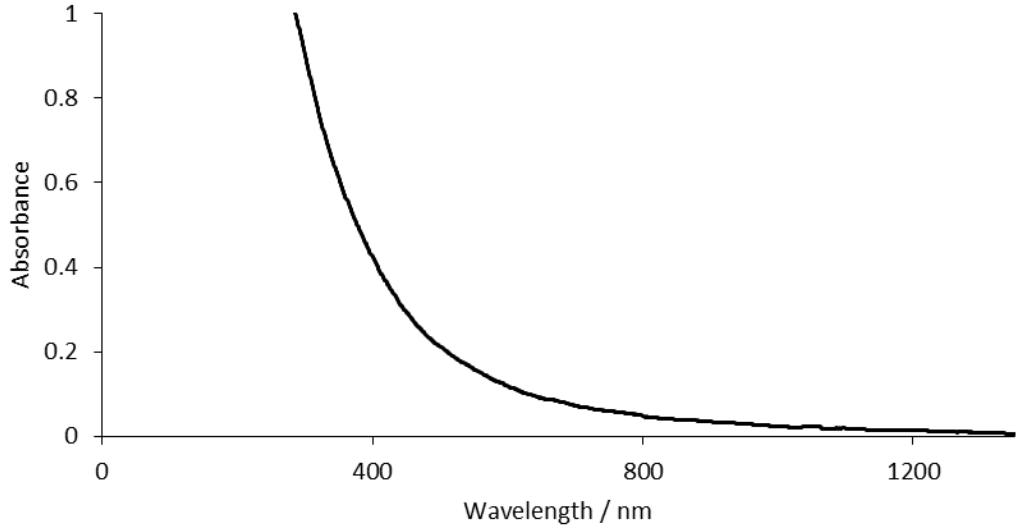

Figure 3.23. UV-vis spectra for unwashed platinum/PVP nps, recorded in ethanol at 1mg mL^{-1} concentration. Spectra are shown up to 1350 nm due to the detection limit of the instrument.

UV-vis spectroscopy for platinum/PVP nps indicated that the use of a higher laser excitation wavelength, might be expected to reduce fluorescent background in Raman spectra. The lower adsorption of the polyvinylpyrrolidone alone or vinylpyrrolidone monomer suggests the fluorescence is more likely to occur when the nanoparticles and polyvinylpyrrolidone are combined, while the effect of varying amount of polyvinylpyrrolidone (as a result of washing) suggests the polyvinylpyrrolidone contributes to the absorbance, and possibly provides pathways leading to more fluorescence.

3.4.3. Gel permeation chromatography (GPC) analysis

GPC analysis was recorded for the as purchased polyvinylpyrrolidone, in order to investigate the chain length of the polymer. This could impact the particle packing of the nanoparticles for study by TIR Raman spectroscopy, and also the synthesis protocol used.[32] Figure 3.24 A-C shows the calibration and GPC traces obtained using two different detection methods, a refractive index (RI) detector, and a right angled light scattering detector (RALS). Calibration was made against polystyrene. Bergius *et al.* demonstrates that there is a precedent for the use of polystyrene standards to calibrate retention volumes for polyvinylpyrrolidone.[39] Both detection methods show a peak at a retention volume of 14.4 mL. The disturbances around 20 mL in the RI detector are likely the result of small molecules, solvent contaminants, or injection effects and come below the region in which polymer molecular weights are expected to fall. It should be noted that for RALS detection, the instrument was positioned under a fan which caused excess background noise, and degraded the signal available.

RI detection (calibrated in the range displayed in Figure 3.24 A) gave a moderately high polydispersity index (PDI) of 3.65, a measure of the range over which the polymer M_w varies. For both RALS and RI detection the likely M_w of the polyvinylpyrrolidone (11,725 g mol^{-1} obtained by RI GPC detection in both cases and the calibrated retention volume) varied significantly from the 55,000 g mol^{-1} quoted by Sigma Aldrich. The method used by Sigma Aldrich to obtain the M_w value was not specified.

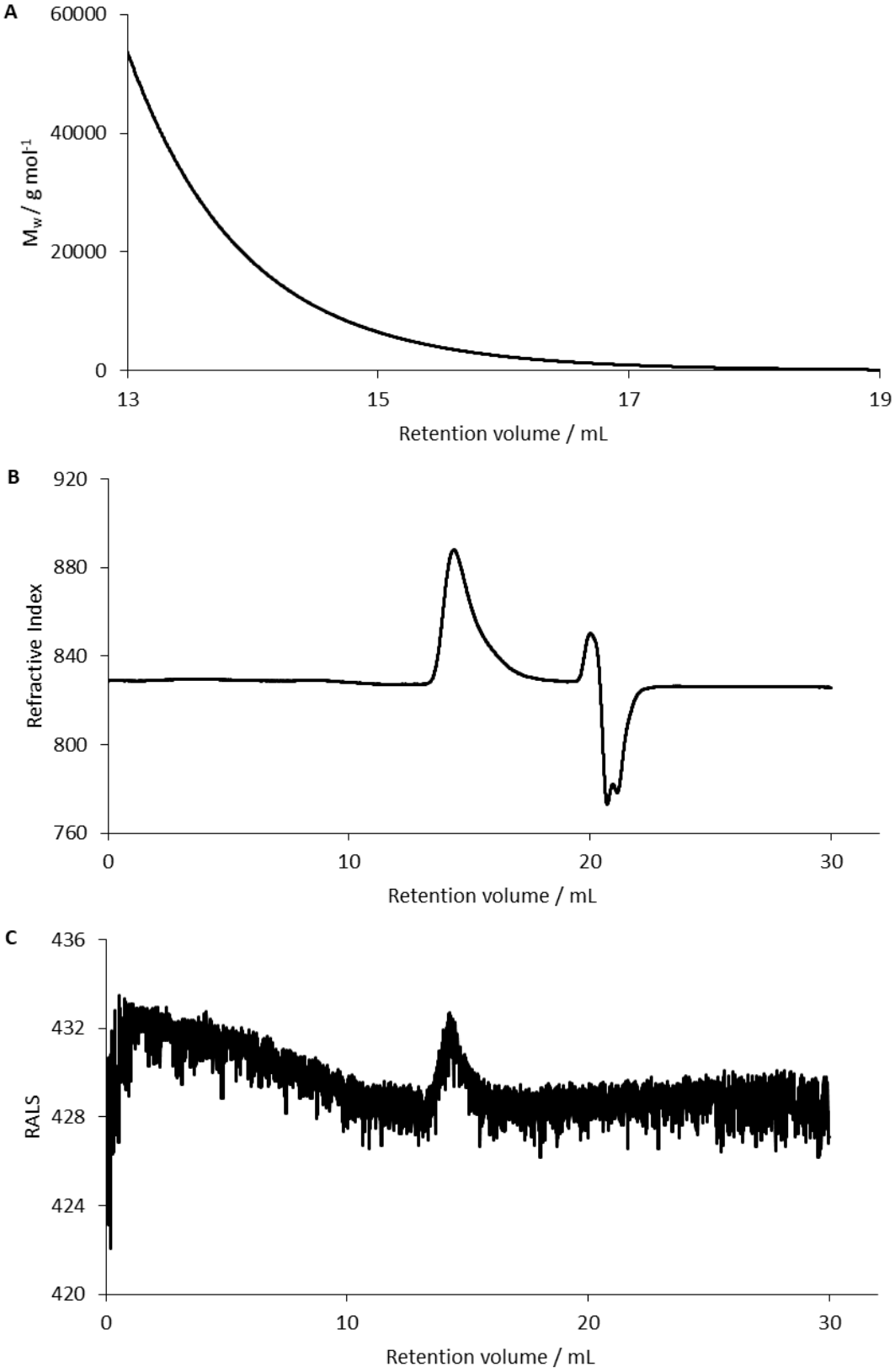

Figure 3.24. GPC RI calibration (A) and data from RI and RALS detection methods (B, C) for polyvinylpyrrolidone as obtained from Sigma Aldrich.

3.4.4. Soxhlet purification

In parallel to trying to understand the origin of fluorescence from platinum/PVP nps with UV-vis, impurities in the polyvinylpyrrolidone were thought to contribute and a purification technique was sought to try and reduce the concentration of any contamination in the material received from Sigma Aldrich. Soxhlet extraction was selected as a means of purification of the polyvinylpyrrolidone capping agent with a view to determining whether impurities might be linked to the observed Raman fluorescence. Hence the UV-vis spectra of Soxhlet purified samples was also recorded.

Soxhlet extraction was first performed using a thimble in water, but was unsuccessful due to the solubility of polyvinylpyrrolidone in water. The extraction was repeated using a dialysis bag to prevent polyvinylpyrrolidone from passing out of the upper reservoir. UV-vis and NMR analysis were recorded for the product obtained *via* the dialysis bag method (no analysis was recorded for the unsuccessful thimble extraction). A small tear at the top of the dialysis bag allowed a small amount of material to make contact with the water, and so was collected with the water in the bottom vessel (Figure 3.25 top Spectrum). Although unintended, this material provided a reference and so was isolated to allow a comparison of the purity between the material in the dialysis bag and that which remained unwashed, but treated *via* the same wetting/drying process. UV-vis results for material which had passed through the dialysis bag are given in Figure 3.25 bottom spectrum. The sample which passed through the dialysis bag showed a lower absorbance in range 0 to 1500 nm. The higher purity and lower absorption intensity seen had been expected. This would be anticipated to lead to lower levels of Raman fluorescence. Comparison of “Soxhlet dialysis purified sample”, Figure 3.25 bottom spectrum, to sample prior to purification, Section 3.4.2 Figure 3.21 bottom Spectrum, showed marginally greater absorbance for the as purchased polyvinylpyrrolidone than the purified polyvinylpyrrolidone. This fitted with the expected increase in UV-vis absorbance for material, which was likely to have contained impurities. ^{13}C and ^{1}H NMR spectroscopy, given in the Appendix also showed inconclusive results as to whether purification had caused any discernible chemical change to the polyvinylpyrrolidone purity. However, as the changes were small after attempted purification, the overall finding that polyvinylpyrrolidone was consistently causing large fluorescent backgrounds was used to instead direct subsequent synthetic efforts to use capping agents for which fluorescence was not seen.

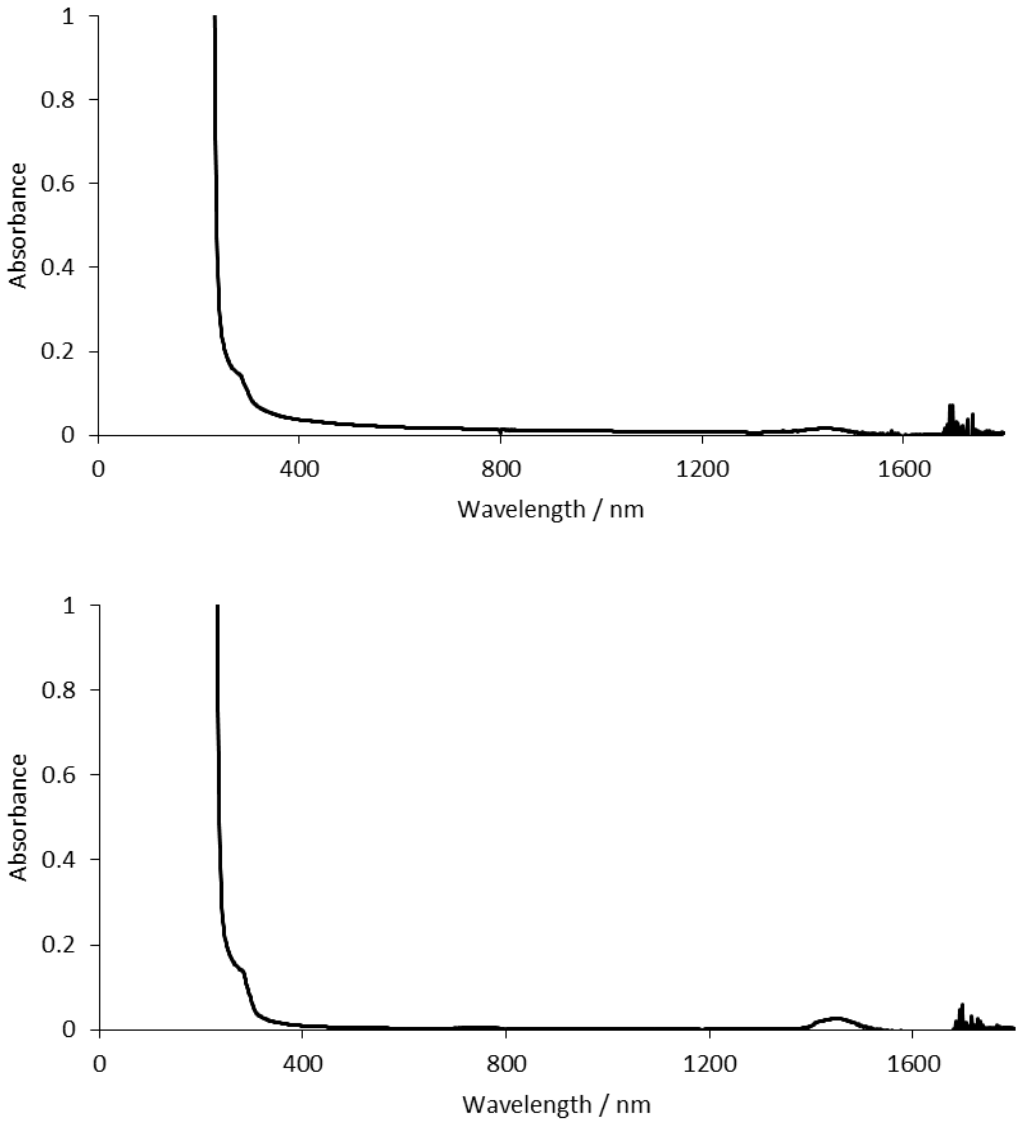

Figure 3.25. UV-vis spectra for dialysis extraction of polyvinylpyrrolidone (Section 2.2.2). Top: material prior to purification, collected from the bottom flask which had not passed through the dialysis bag. Bottom: material after purification which had passed through the dialysis bag. Both with a concentration of 1mg mL^{-1} in ethanol (data average of three sets).

3.5. Proof of concept detection of nanoparticle capping agent using TIR Raman spectroscopy

Capping agents provide a readily available source of absorbed molecules, since they are already present on the as prepared nanoparticles. In this work we took advantage of this fact as a starting point for comparing TIR Raman against the confocal Raman spectroscopy described above.

3.5.1. TIR Raman spectroscopic studies of platinum/PVP nps

In the first instance, the platinum/PVP nps investigated above using confocal Raman were investigated using TIR Raman spectroscopy. An increase in sensitivity and a reduction in the high fluorescent background seen by confocal Raman spectroscopy was a key aim of this study. TIR Raman spectra are given in Figures 3.26 and 3.27 and were recorded for platinum/PVP nps deposited at a monolayer concentration on a silicon hemisphere using LB deposition. No spectral features were seen, across the regions of interest.[31]

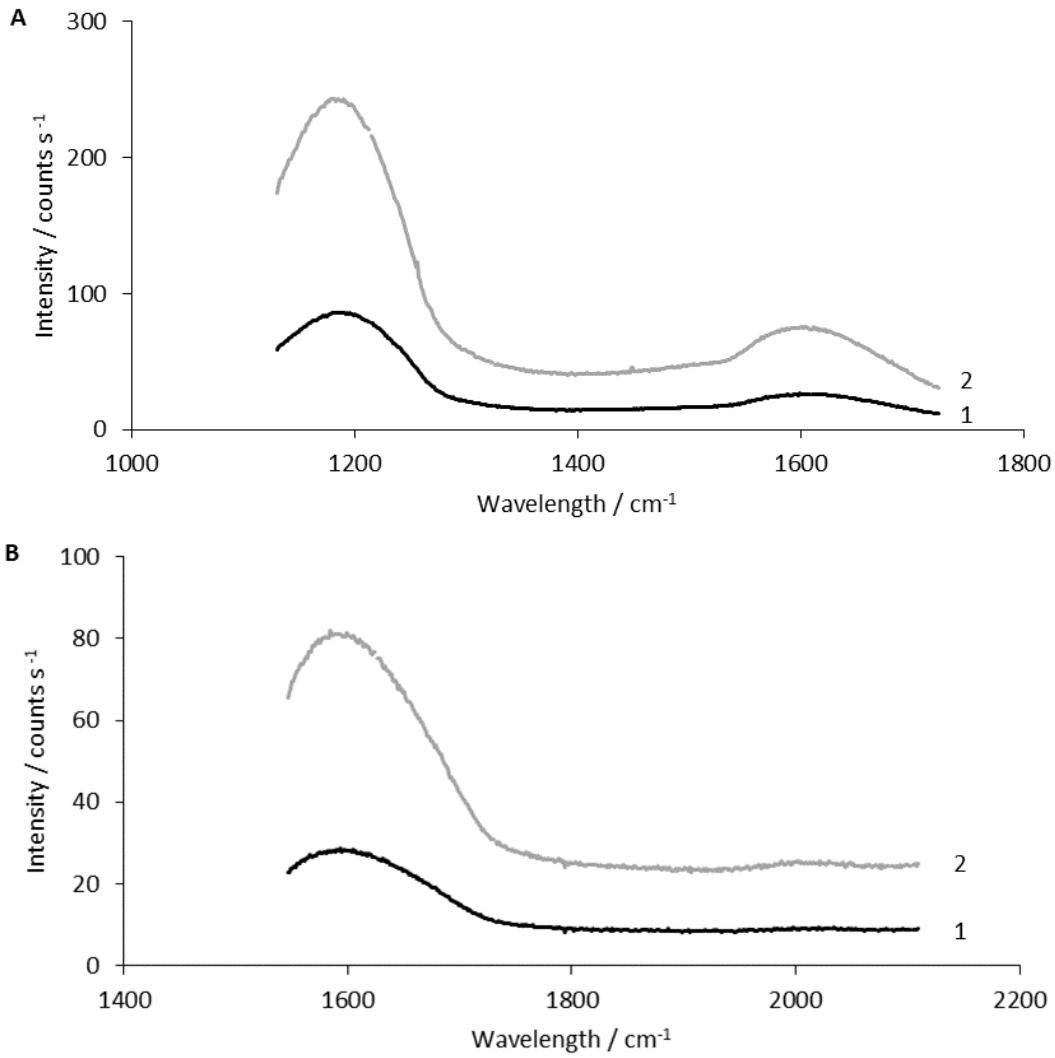

Figure 3.26. TIR Raman spectra for 1- clean silica hemisphere, 2- platinum/PVP nps LB deposited at a monolayer concentration on a silica hemisphere. Spectra were recorded for three regions (Figure 3.26 A-B, Figure 3.27 A) at which spectral features were expected,[31] with a 532 nm excitation wavelength. Spectra were recorded on System 2 under the standard conditions described in Section 2.2.4.2, with 10 lots of 5 s acquisitions recorded. Spectra were offset vertically for clarity. Single point data, attributed to stray electronic signals, have been removed as part of data processing.

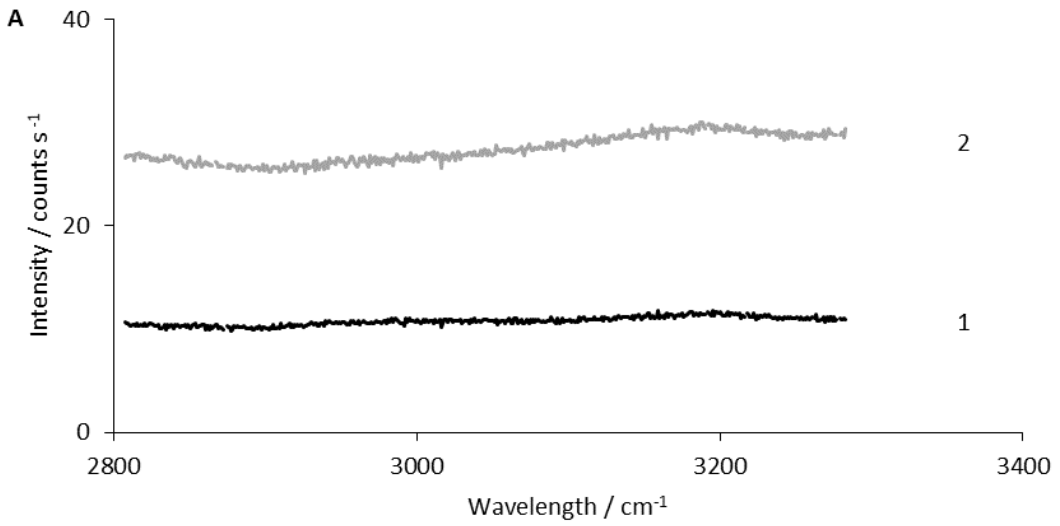

Figure 3.27. TIR Raman spectra for 1- clean silica hemisphere, 2- platinum/PVP nps LB deposited at a monolayer concentration on a silica hemisphere. Spectra were recorded for three regions (Figure 3.26 A-B, Figure 3.27 A) at which spectral features were expected,[31] with a 532 nm excitation wavelength. Spectra were recorded on System 2 under the standard conditions described in Section 2.2.4.2, with 10 lots of 5 s acquisitions recorded. Spectra were offset vertically for clarity. Single point data, attributed to stray electronic signals, have been removed as part of data processing.

3.5.2. TIR Raman studies of silver/OAm/OAc nps

TIR Raman spectra were recorded for a deposited monolayer sample of silver/OAm/OAc nps. In order to allow for assignment of such spectra, the corresponding bulk spectra were recorded for both capping agents supported in a capillary tube and recorded on Raman spectroscopic System 3 (as described in Chapter 5). Spectra are given in Figure 3.28, and expected literature bands, for both capping agents, along with those obtained experimentally are tabulated in Tables 3.6-3.9. It should be noted that since these bulk capping agent samples were not deposited upon a silica hemisphere, as all TIR Raman samples are, no support interactions would be expected. This should be considered when assigning the TIR Raman spectra. TIR Raman spectra recorded of the regions in which features were expected are given in Figures 3.29 and 3.30, with full assignments given in Table 3.10. The peak centred on 1160 cm^{-1} was attributed to C-C stretching bond.[40] For the spectra centred around 1400 cm^{-1}, two peaks were seen, centred around 1375 cm^{-1} and 1610 cm^{-1}. These were assigned to stretching of the C=C in the organic capping agent, this could be oleylamine or oleic acid, as this band would be present for both.[40] The peak centred at 1610 cm^{-1} could also be assigned to the bending vibration in NH_2 in oleylamine. The three bands centred around 2910, 2930, 2970 cm^{-1} were assigned to the CH_2 symmetrical stretch, and the C-H stretch in CH=CH respectively.[40] The band seen at 3170 cm^{-1} was not assigned, although it is possible that interaction between the nanoparticles and the silica support could

be responsible for these unassigned features. In all the spectra obtained for a monolayer sample of silver/OAm/OAc nps on the silica hemisphere substrate demonstrate the organic capping agent can be detected. However, deduction of whether oleylamine or oleic acid capping agent was surrounding the metal in this dual capped system was not possible, owing to the similarity of the bands observed to those for both oleylamine and oleic acid It should be noted that silver is known to be a SERS active metal, however the size of the particles is sufficiently small that they should not be SERS active.[41] Nevertheless a distribution of particle sizes could be present and SERS activity cannot be entirely ruled out. The next stage is therefore to look at the same type of capping agents on a non-coinage metal to rule out the possibility of SERS enhancements.

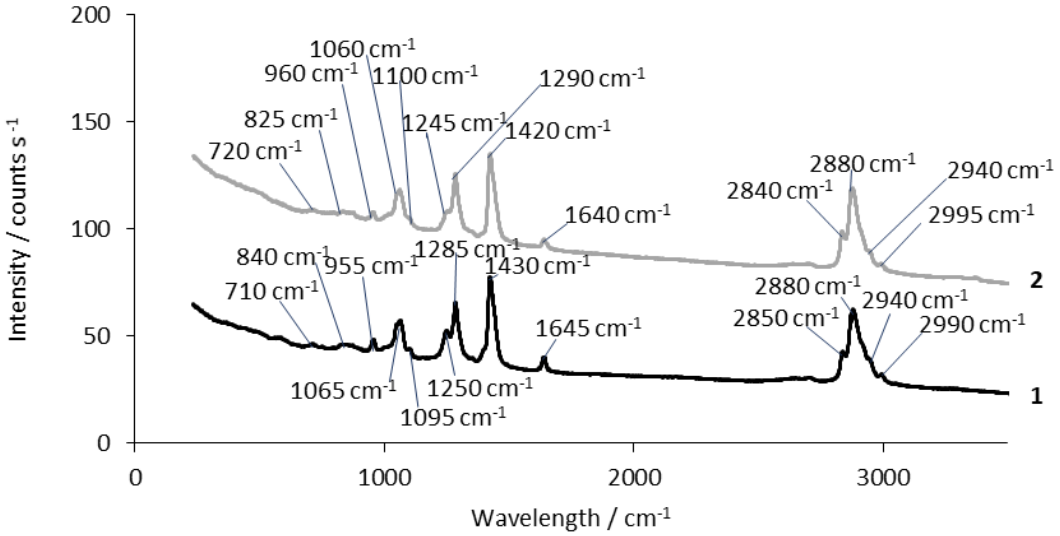

Figure 3.28. Bulk TIR Raman spectra taken for the following capping agents within a capillary tube: 1- oleic acid, 2- oleylamine. Spectra were taken on System 3 (Section 2.2.4.3) at a laser power set at 200 mW for 10 frames taken with a 10 s exposure time. All spectra were taken using grating 3 with a slit width of 100 µm. Spectra have been offset vertically for clarity. Single point data, attributed to stray electronic signals, have been removed as part of data processing.

*Table 3.6. Literature values for expected Raman stretching frequencies for **oleic acid**.*[40] *Where, sym=symmetrical mode, and str=stretch.*

Vibrational mode	**Wavelength / cm^{-1}**
C-C str	1052, 1073,1105,1254
C=C	1292,1646
C-H str	1428, 1449, 2719
CH_2 ν-sym	2843
CH_3 ν-sym	2866
C-H str (in CH=CH)	3000

*Table 3.7. Literature values for expected Raman stretching frequencies for capping agent **oleylamine**.*[11,12] *Where vs=symmetric stretching vibration, vas=asymmetric stretching vibration, def=deformation*, δ=bending vibration.

Literature vibrational mode	**Frequency / cm^{-1}**
vs(C-C)	722
vs(C-N)	1071
δ(CH_3)	1465
δ(NH_2)	1604, 795
vs(C=C)	1647
vas(C-H) and vs(C-H)	2925, 2853
vs (=C-H)	3004
vs(N-H)	3300
vas(NH_2) and vs(NH_2)	3376, 3295

*Table 3.8. Assignment of Raman stretching frequencies for **bulk oleic acid** spectra recorded in a capillary tube as shown in Figure 3.28 spectra 1. Where, sym=symmetrical mode, str=stretch.*

Vibrational mode	**Wavelength / cm^{-1}**
unassigned	710,840,955
unassigned	2880
unassigned	2940
C-C str	1065
C-C str	1095,1250
C=C	1285
C-H str	1430
C=C	1645
CH_3 ν-sym	2850
C-H str (in CH=CH)	2990

*Table 3.9. Assignment of Raman stretching frequencies for **bulk oleylamine** spectra recorded in a capillary tune as shown in Figure 3.28 spectra 2. Where vs=symmetric stretching vibration, vas=asymmetric stretching vibration,* and δ=bending vibration.

Vibrational mode	**Wavelength / cm^{-1}**
vs(C-C)	720
δ(NH_2)	825
unassigned	960
vs(C-N)	1060
unassigned	1100,1245,1290
δ(CH_3)	1420
vs(C=C)	1640
vs(C-H)	2840
unassigned	2880
vas(C-H)	2940
vs (=C-H)	2995

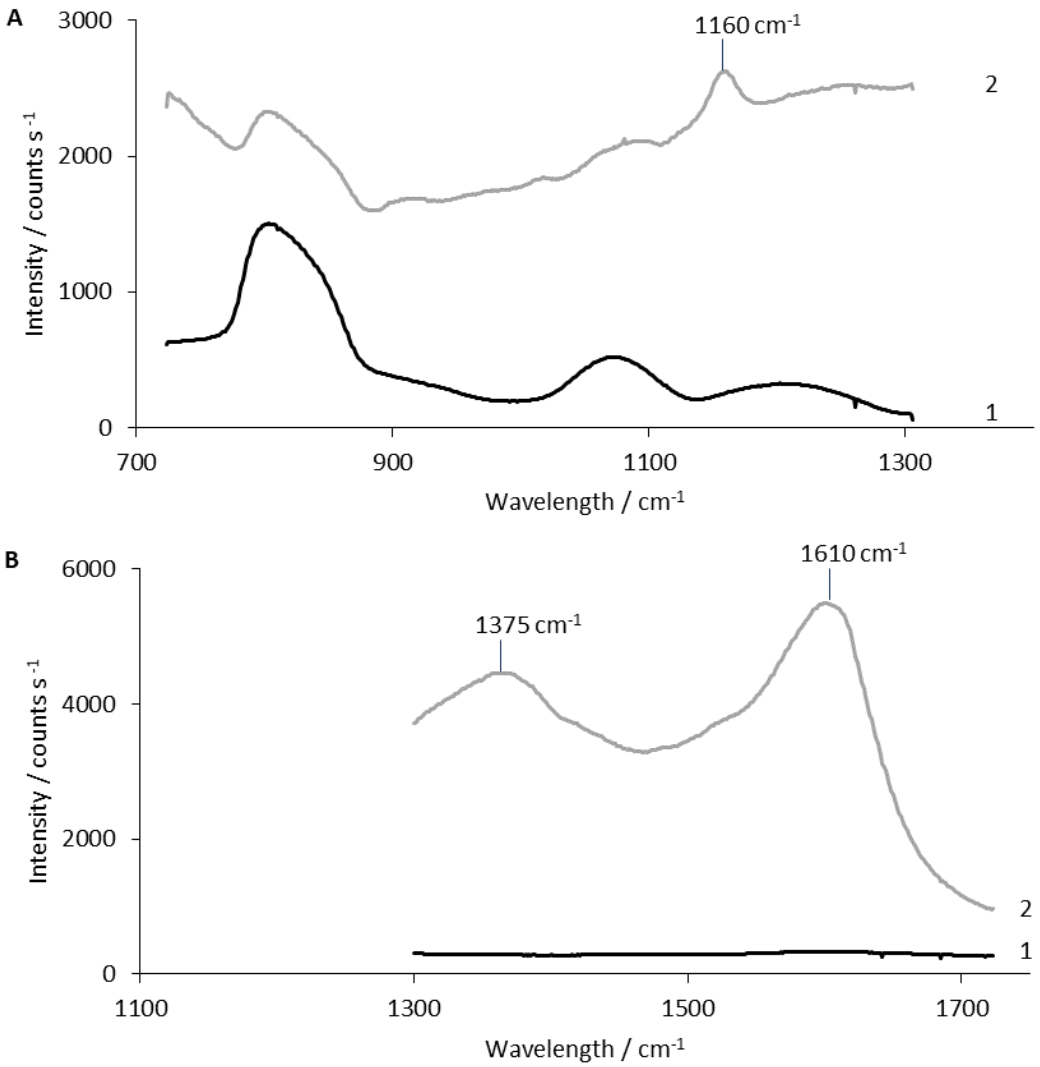

Figure 3.29. TIR Raman spectra with a 532 nm excitation wavelength of 1- clean silica hemisphere, 2- silver/OAm/OAc nps LB deposited at a monolayer concentration on a silica hemisphere. Spectra were recorded for three regions (Figure 3.29 A-B, Figure 3.30 A) at which spectral features were expected (Figure 3.28, and Table 3.7 and 3.8). Spectra were recorded on System 2 under the standard conditions described in Section 2.2.4.2. 10 lots of 5 s acquisitions were recorded for spectra 1 and 2. Single point data, attributed to stray electronic signals, have been removed as part of data processing.

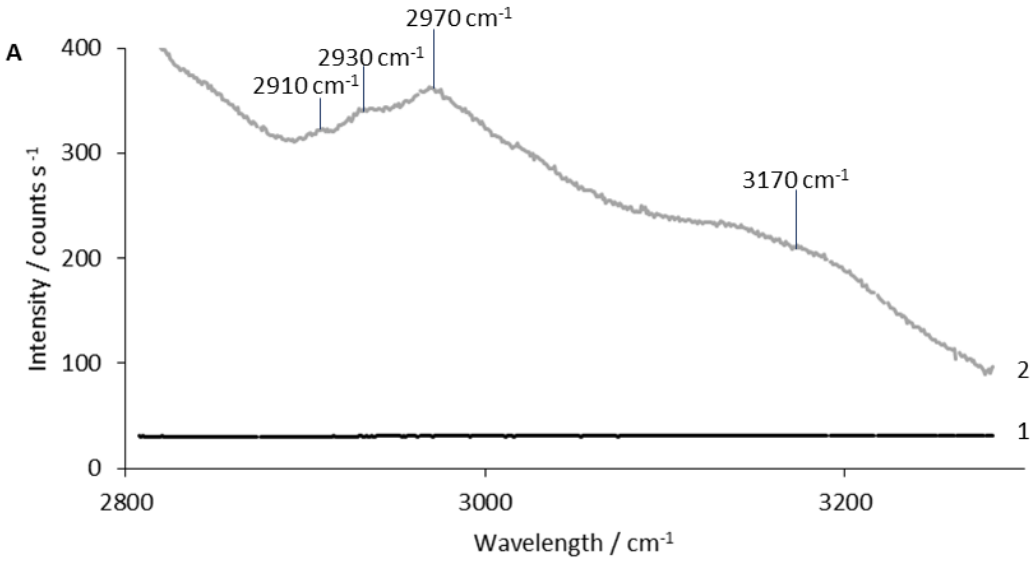

Figure 3.30. TIR Raman spectra with a 532 nm excitation wavelength of 1- clean silica hemisphere, 2- silver/OAm/OAc nps LB deposited at a monolayer concentration on a silica hemisphere. Spectra were recorded for three (Figure 3.29 A-B, Figure 3.30 A) regions at which spectral features were expected (Figure 3.26, and Table 3.7 and 3.8). Spectra were recorded on System 2 under the standard conditions described in Section 2.2.4.2. 10 lots of 5 s acquisitions were recorded for spectra 1 and 2. Single point data, attributed to stray electronic signals, have been removed as part of data processing.

Table 3.10. Assignment of Raman stretching frequencies for oleylamine (OAm) and oleic acid (OAc) for TIR Raman spectra for monolayer silver/OAm/OAc np deposited samples on a silica hemisphere as shown in Figures 3.29 and 3.30. Where, sym=symmetrical mode, str=stretch, δ = bending vibration, *and N/A is given when no bands fitting this vibrational mode were seen.*

Vibrational mode OAm	**Vibrational mode OAc**	**Wavelength / cm^{-1}**
unassigned	**unassigned**	2930
unassigned	**unassigned**	3170
unassigned	**C-C str**	1160
unassigned	**C=C, or C-H str**	1375
δ(NH_2)	**C=C**	1610
vas(C-H)	**CH_3 ν-sym**	2910
vs (=C-H)	**C-H str (in CH=CH)**	2970

3.5.3. TIR Raman studies of palladium/OAm nps

Palladium nanoparticles were investigated using TIR Raman. Palladium is not a coinage metal and does not typically result in SERS enhancement of Raman scattering. The palladium system also uses only one capping agent and so might help discrimination of oleic acid and

oleylamine bound to the nanoparticle for systems such as silver/OAm/OAc. Assignment of the capping agent could be made from Figures 3.29 and 3.30 Spectrum 2 and Tables 3.6-3.9. TIR Raman spectra of the palladium/OAm nps, for regions at which features were expected, are given in Figures 3.31 and 3.32. The 1160 cm^{-1} and 1650 cm^{-1} bands, seen for the silver/OAm/OAc nps and attributed to C-C and C=C stretching, were not seen in these spectra. The 1350 cm^{-1} band (here centred round 1290 cm^{-1}), assigned to the C=C stretch was seen, for both the silver and palladium nanoparticles. Though the intensity of this band was low in the palladium Raman spectrum. Peaks were also seen, centred around 1485 cm^{-1} (again very weak), and around 2970 cm^{-1} (with a shoulder at 2930 cm^{-1}) and 3020 cm^{-1} (both stronger) and were assigned as the C-H stretch, CH_3 symmetric stretch and C-H stretch (for the CH=CH bond) respectively.[40] Differences in the bands detected were seen for the silver and palladium systems. These differences might indicate that the identity or the bonding of the capping agent at the metal surface was not the same for the silver and palladium nanoparticles. Therefore it could tentatively be suggested that oleic acid was predominantly present at the surface of the silver nanoparticles.

The relative intensity of the features on the palladium and silver particles possibly suggest the silver system could have some enhancement from SERS, since much larger peaks in the 1290 cm^{-1} case seem to be present, assuming this is correctly assigned to C=C in both cases. Nevertheless the clear features for oleylamine on the surface of the palladium nanoparticles point to the effectiveness of TIR Raman spectroscopy for measuring surface species on the nanoparticle monolayer even in the absence of any SERS contribution. Given the observation of the peaks (centred on 1290, 1485, 2930, 2970, and 3020 cm^{-1}), it may be useful to employ the plasma cleaning protocol (see Section 3.6 below). If reduction or removal of these bands, was seen upon plasma cleaning (where removal of the organic capping agent is expected), then the assignment of these to surface bound capping agent may be confirmed.

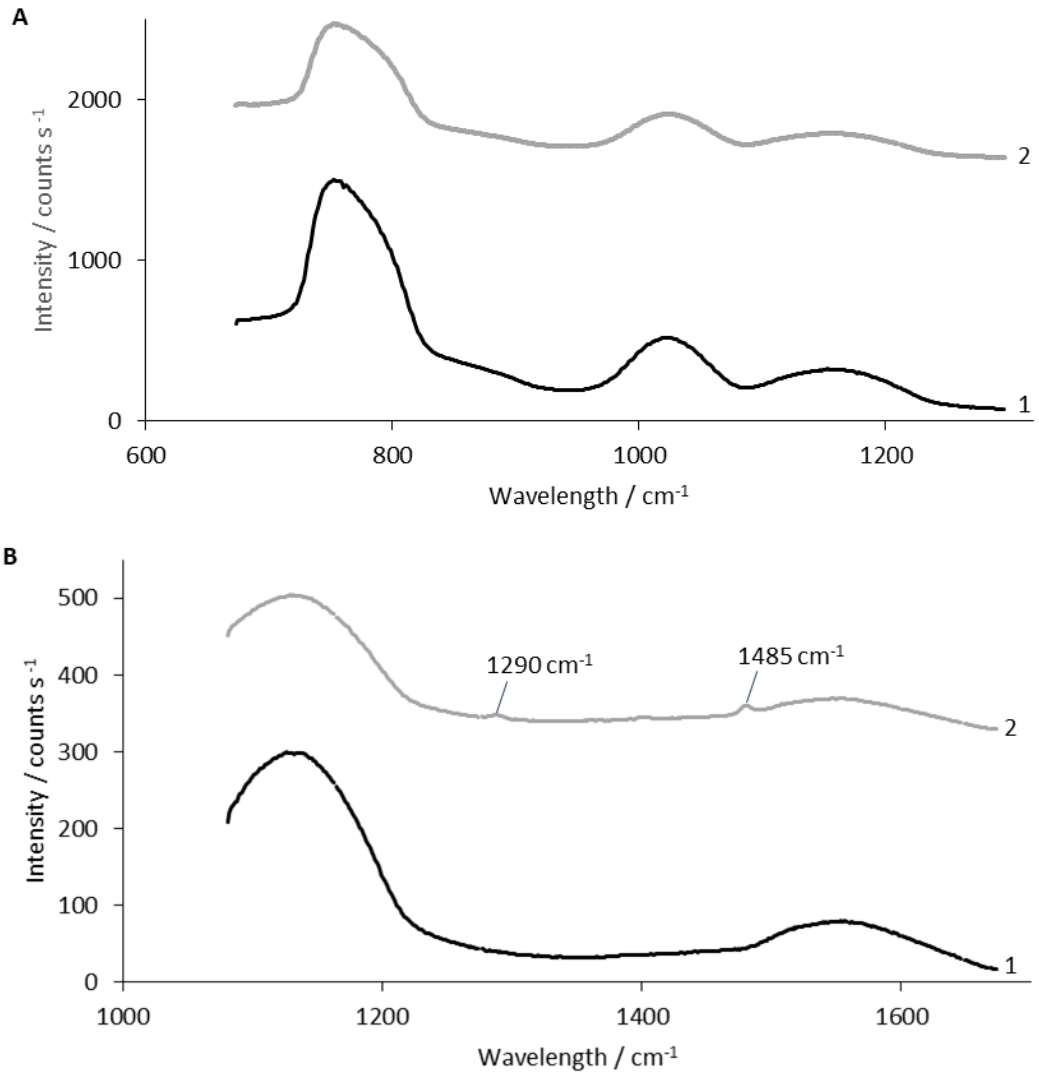

Figure 3.31. TIR Raman spectra for 1- clean silica hemisphere, 2- palladium/OAm nps LB deposited onto a silica hemisphere. Spectra in Figure 3.31 A-B and 3.32 A were taken across three differing regions of wavelength, with 532 nm excitation wavelength. Spectra were recorded on System 2 under the standard conditions described in Section 2.2.4.2. 10 lots of 5 s acquisitions were recorded for spectra 1 and 2. All Spectra offset for clarity. Single point data, attributed to stray electronic signals, have been removed as part of data processing.

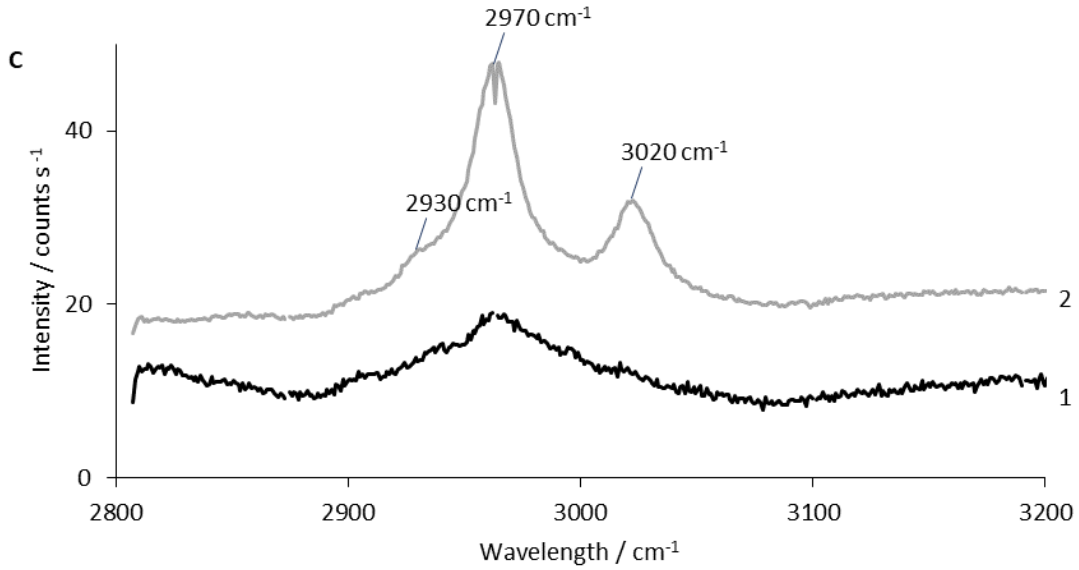

Figure 3.32. TIR Raman spectra for 1- clean silica hemisphere, 2- palladium/OAm nps LB deposited onto a silica hemisphere. Spectra in Figure 3.31 A-B and 3.32 A were taken across three differing regions of wavelength, with 532 nm excitation wavelength. Spectra were recorded on System 2 under the standard conditions described in Section 2.2.4.2. 10 lots of 5 s acquisitions were recorded for spectra 1 and 2. All Spectra offset for clarity. Single point data, attributed to stray electronic signals, have been removed as part of data processing.

3.6. Development of plasma cleaning protocol for capping agent removal.

For catalytic and spectroscopic applications, it is often desirable to have a clean surface. Plasma cleaning was therefore investigated to allow removal of capping agents that gave rise to the TIR Raman bands. Plasma generates ions and radicals that cause the dissociation of molecular bonds that would not typically break up under the same conditions thermally. These organic fragments, in the presence of a gas flow or vacuum should then be removed from the metal-silica surface. The amount of time samples were plasma cleaned for was investigated. TIR Raman spectroscopy was then used to monitor the removal of the bands attributed to the capping agent.

3.6.1. Platinum/PVP nps

TIR Raman spectra taken for the platinum/PVP nps, deposited at a monolayer concentration on a silica hemisphere after plasma cleaning for 120 s, is given and compared to those of the clean hemisphere and the as deposited sample (Figures 3.33 and 3.34). After 120 s of plasma cleaning no change was seen for the TIR Raman spectra recorded compared to that of the as deposited sample. This further validated the assignment of no spectral features for the monolayer platinum/PVP np sample (Section 3.5.1, Figures 3.26 and 3.27).The plasma cleaning time was selected based upon the SEM imaging described below (Section 3.6.1.1).

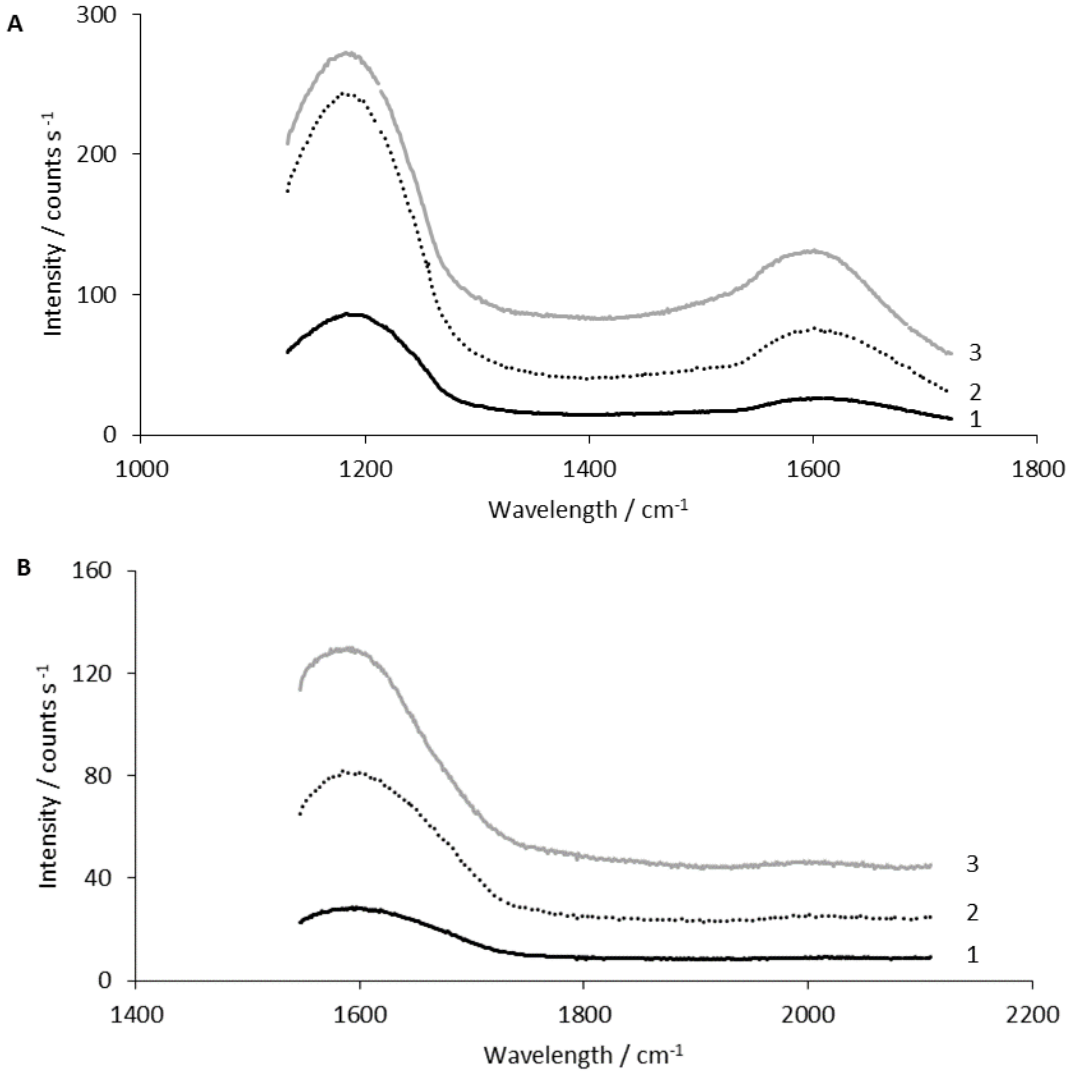

Figure 3.33. TIR Raman spectra for 1- clean silica hemisphere, 2- platinum/PVP nps LB deposited at a monolayer concentration on a silica hemisphere, 3- sample 2 plasma cleaned for 120 s. Spectra were recorded for three regions (Figure 3.33 A-B, Figure 3.34 A) at which spectral features were expected,[31] *with a 532 nm excitation wavelength. Spectra were recorded on System 2 under the standard conditions described in Section 2.2.4.2. 10 lots of 5 s acquisitions were recorded. Spectra offset vertically for clarity. Single point data, attributed to stray electronic signals, have been removed as part of data processing.*

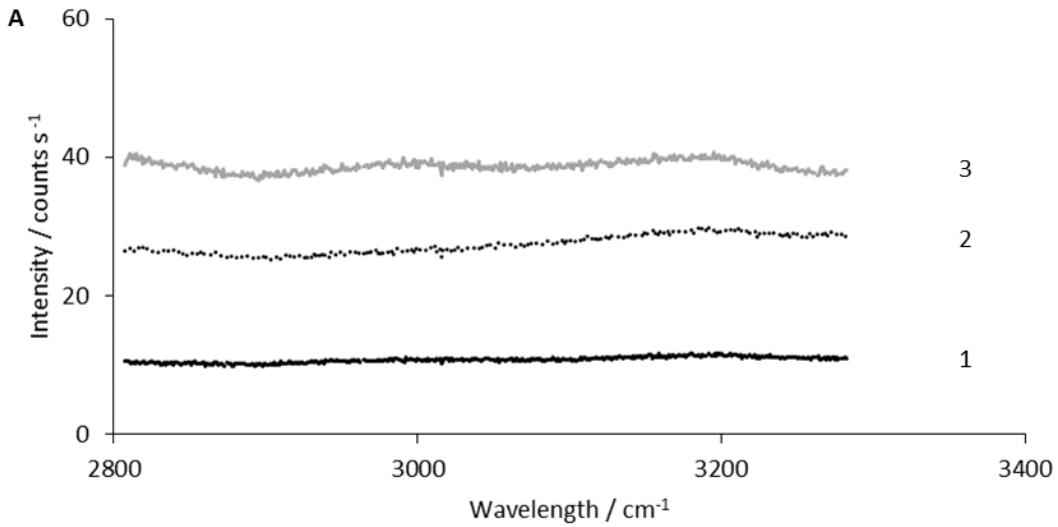

Figure 3.34. TIR Raman spectra for 1- clean silica hemisphere, 2- platinum/PVP nps LB deposited at a monolayer concentration on a silica hemisphere, 3- sample 2 plasma cleaned for 120 s. Spectra were recorded for three regions (Figure 3.33 A-B, Figure 3.34 A) at which spectral features were expected,[31] with a 532 nm excitation wavelength. Spectra were recorded on System 2 under the standard conditions described in Section 2.2.4.2. 10 lots of 5 s acquisitions were recorded. Spectra offset vertically for clarity. Single point data, attributed to stray electronic signals, have been removed as part of data processing.

3.6.1.1. SEM investigation of LB deposited materials

SEM imaging (Figure 3.35) was used to monitor the appearance and morphology of the supported platinum/PVP nps, after plasma cleaning. Imaging took place after plasma cleaning in order to allow removal of the thick layer of surface carbon which would likely to prohibit imaging or require additional coating of the sample. A 2 min plasma cleaning time was selected, as this represents a relatively long cleaning period. SEM imaging showed a relatively uniform surface, with no indication of agglomeration of the metal nanoparticles, upon capping agent removal. Evaluation of the image gives a surface coverage, for platinum metal, of around 25%.

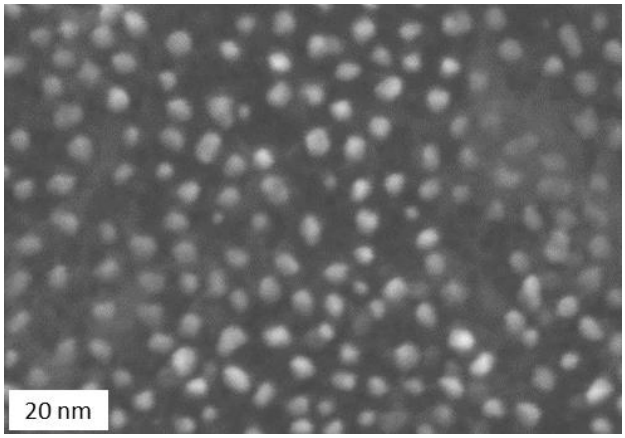

Figure 3.35. SEM image for platinum/PVP nps deposited using LB deposition (1 layer) on a silicon wafer, plasma cleaned for 2 min to facilitate removal of the organic capping agent.

3.6.2. Silver/OAm/OAc nps

For silver nanoparticles a variety of bands were detected using TIR Raman and attributed to the capping agent or possible interaction of the nanoparticle and support. Spectra for plasma cleaning of the supported silver/OAm/OAc nps on a silica substrate are given in Figures 3.36 and 3.37. The band centred at 1160 cm^{-1}, and attributed to the C-C bond on the capping agent, was removed by plasma cleaning for 60 s. For a longer 120 s plasma cleaning time, low frequency peaks at 945, 1010, and 1090 cm^{-1} appeared (Figure 3.36 A). Similarly, at higher wavelengths some new low intensity bands were also seen after 120 s of plasma cleaning at 1270, 1335, 1370, 1550, and 1690 cm^{-1}. These peaks might be attributed to carbonaceous species formed during plasma cleaning which stay localised on the metal surface. The peaks centred around 1375, and 1650 cm^{-1}, which had been assigned to C=C stretching in the capping agent diminished in intensity as the sample was plasma cleaned for 60 s. This corresponded to partial removal of the organic capping agent. Finally for the three bands centred around 2900, 2950, 3000 cm^{-1}, which were assigned to the CH_2 symmetrical stretch, and the C-H stretch in CH=CH respectively, along with the two unassigned bands at 3150, and 3200 cm^{-1} a slight reduction in intensity was seen after 60 s of plasma cleaning. The longer 120 s plasma cleaning time appeared to give a slight increase in intensity again attributed to carbaneous species formed during plasma cleaning. Therefore, plasma cleaning of silver/OAm/OAc nps, had led to partial but not full capping agent removal.

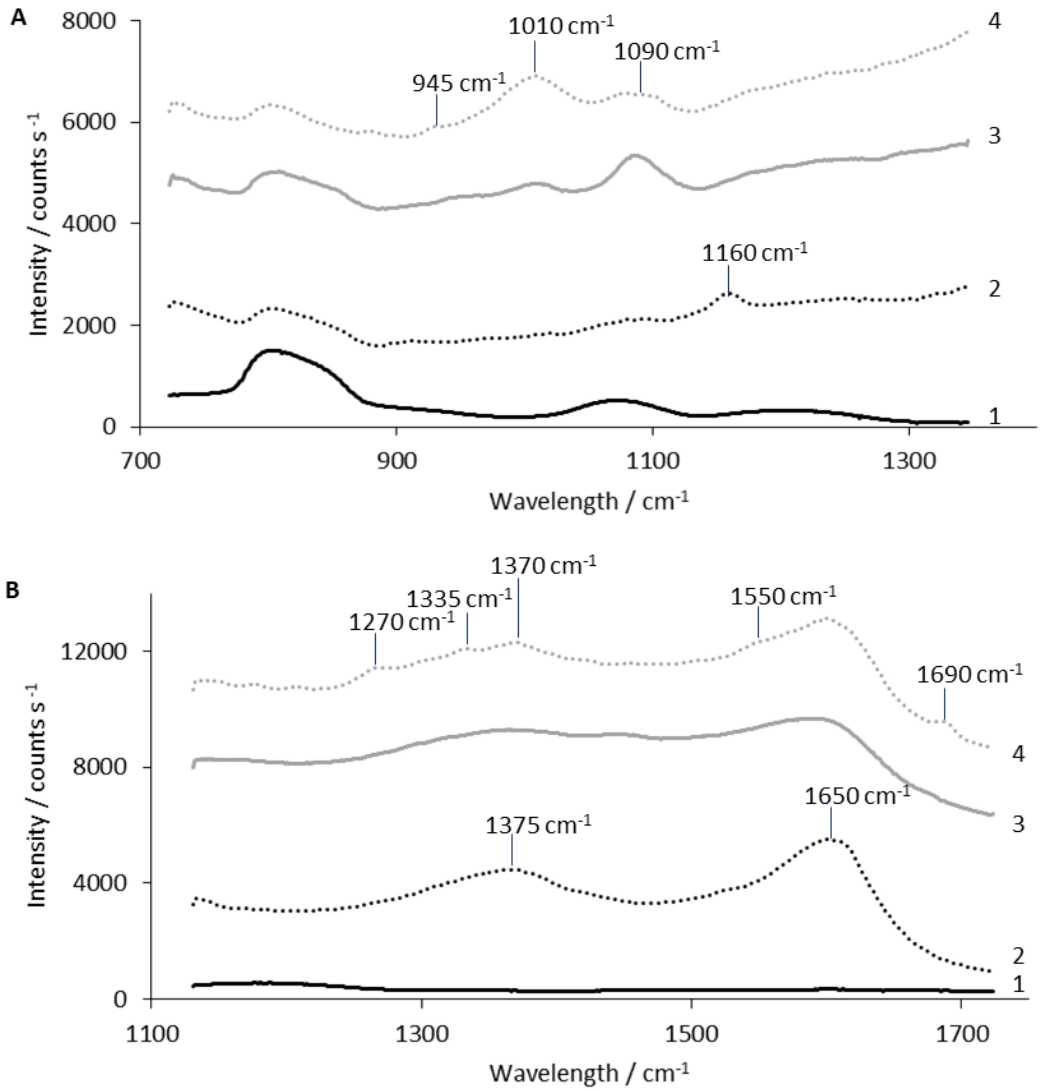

Figure 3.36. TIR Raman spectra for 1- a clean silica hemisphere, 2- silver/OAm/OAc nps LB deposited at a monolayer concentration on a silica hemisphere, 3- sample 2 plasma cleaned for 60 s, 4- sample 2 plasma cleaned for 120 s. Spectra were recorded for three regions (Figure 3.36 A-B, Figure 3.37 A) at which spectral features were expected (Figure 3.27, and Table 3.10), with a 532 nm excitation wavelength. Spectra were recorded on System 2 under the standard conditions described in Section 2.2.4.2. 10 lots of 5 s acquisitions were recorded for Spectra 1 and 2, and 10 lots of 4 s acquisitions were taken for Spectra 3 and 4. Single point data, attributed to stray electronic signals, have been removed as part of data processing.

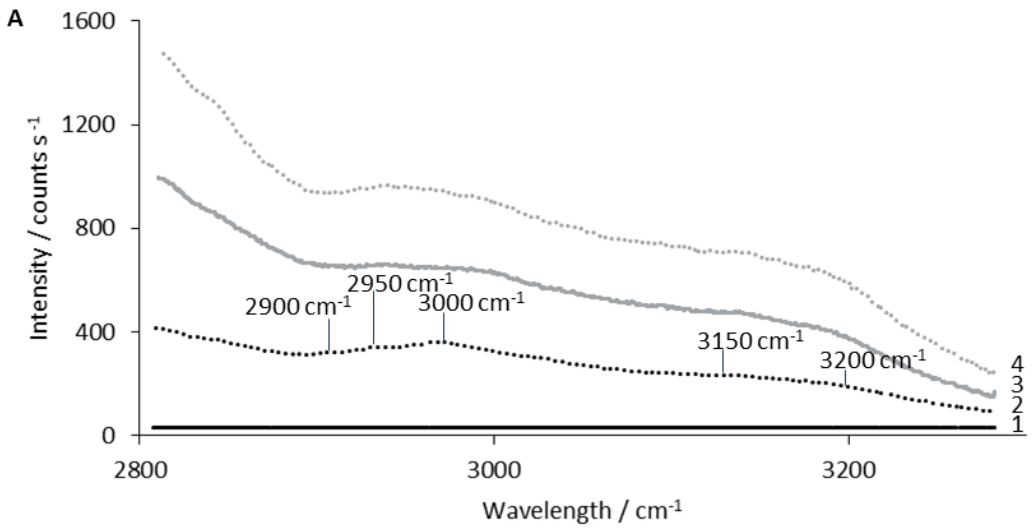

Figure 3.37. TIR Raman spectra for 1- a clean silica hemisphere, 2- silver/OAm/OAc nps LB deposited at a monolayer concentration on a silica hemisphere, 3- sample 2 plasma cleaned for 60 s, 4- sample 2 plasma cleaned for 120 s. Spectra were recorded for three regions (Figure 3.36 A-B, Figure 3.37 A) at which spectral features were expected (Figure 3.27, and Table 3.10), with a 532 nm excitation wavelength. Spectra were recorded on System 2 under the standard conditions described in Section 2.2.4.2. 10 lots of 5 s acquisitions were recorded for Spectra 1 and 2, and 10 lots of 4 s acquisitions were taken for Spectra 3 and 4. Single point data, attributed to stray electronic signals, have been removed as part of data processing.

3.6.3. Palladium/OAm nps

For palladium nanoparticles, four bands had been detected, by TIR Raman spectroscopy for the supported material. Two of these bands had been low in intensity. It was therefore of interest to see if these bands could be reduced in intensity, or completely removed by plasma cleaning. Spectra, for a clean silica hemisphere, deposited palladium/OAm nps, and material plasma cleaned for 20 and 60 s respectively are given in Figures 3.38 and 3.39. For the region of 650 cm^{-1} to 1300 cm^{-1} no bands above the silica background were seen before or after plasma cleaning. For the two low intensity bands, centred on 1290 cm^{-1} and 1485 cm^{-1} and assigned to the C=C and C-H stretching respectively, no reduction in intensity was seen for 20 s of plasma cleaning. However, upon 60 s of plasma cleaning complete removal of both bands was seen. This validated the assignment of these bands, to the capping agent species, which was removed after 60 s of plasma cleaning.

For the bands centre on 2970 cm^{-1} and 3020 cm^{-1}, assigned to CH_3 symmetrical stretching and the C-H stretch in the CH=CH bond respectively, a reduction in Raman intensity was seen upon 20 s of plasma cleaning. Furthermore upon 60 s of plasma cleaning complete removal of both bands was seen. This indicated the desired full removal of the capping agent had been achieved. A clean catalyst surface should result, and spectroscopic data could now

be collected during catalytic runs. Given the similarity in physical properties of platinum and palladium, the stability of the platinum nanoparticles to agglomeration or sintering as observed by SEM for 120 s cleaning indicated it was very likely no significant change to the sample except removal of the organic would occur for palladium either (although a topic for future work to confirm this).

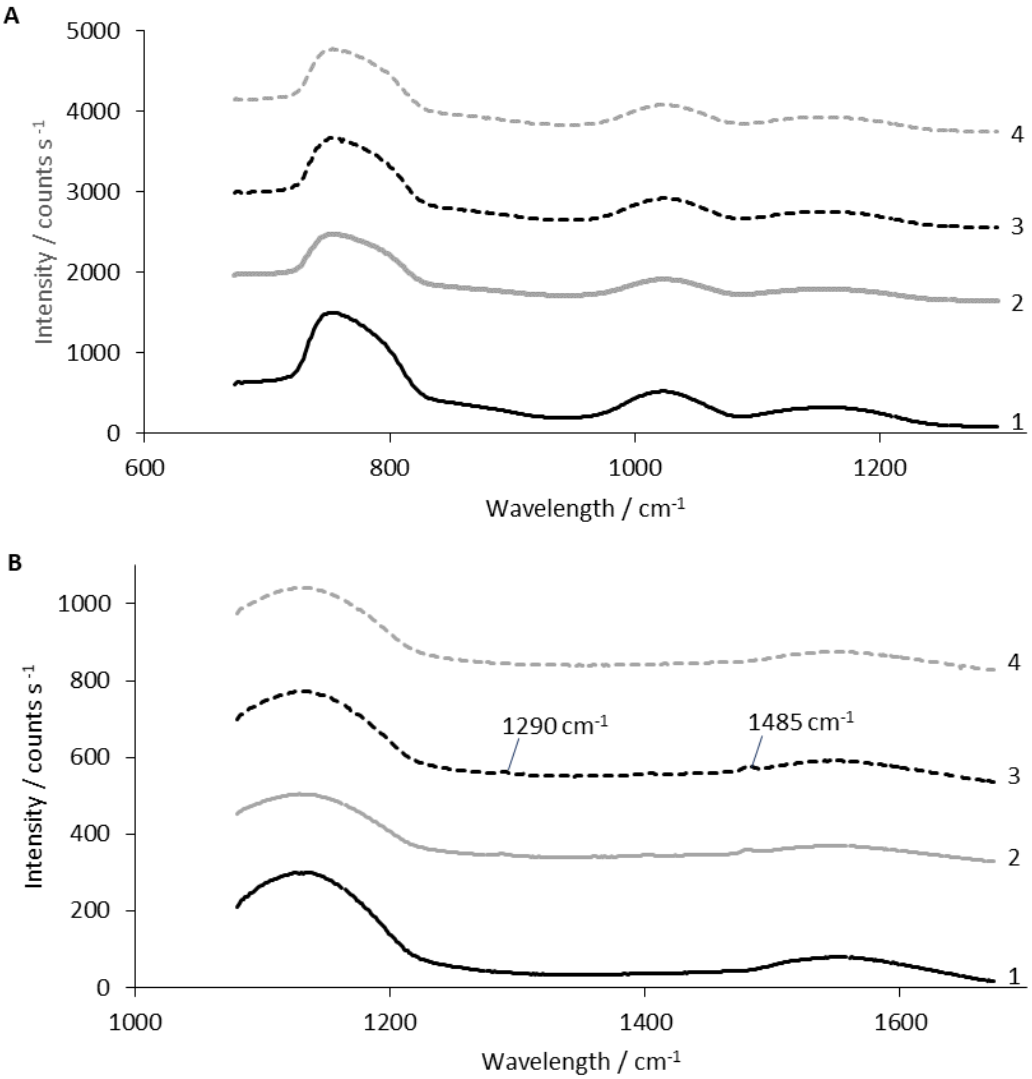

Figure 3.38 .TIR Raman spectra for 1- a clean silica wafer, 2- palladium/OAm nps LB deposited onto a silica wafer, 3- palladium/OAm nps LB deposited onto a silica wafer plasma cleaned for 20 s, 4- palladium/OAm nps LB deposited onto a silica wafer plasma cleaned for 60 s. Spectra taken (Figure 3.38 A-B, Figure 3.39 A) across three differing regions of wavelength, *with 532 nm excitation wavelength. All spectra were offset for clarity. Single point data, attributed to stray electronic signals, have been removed as part of data processing.*

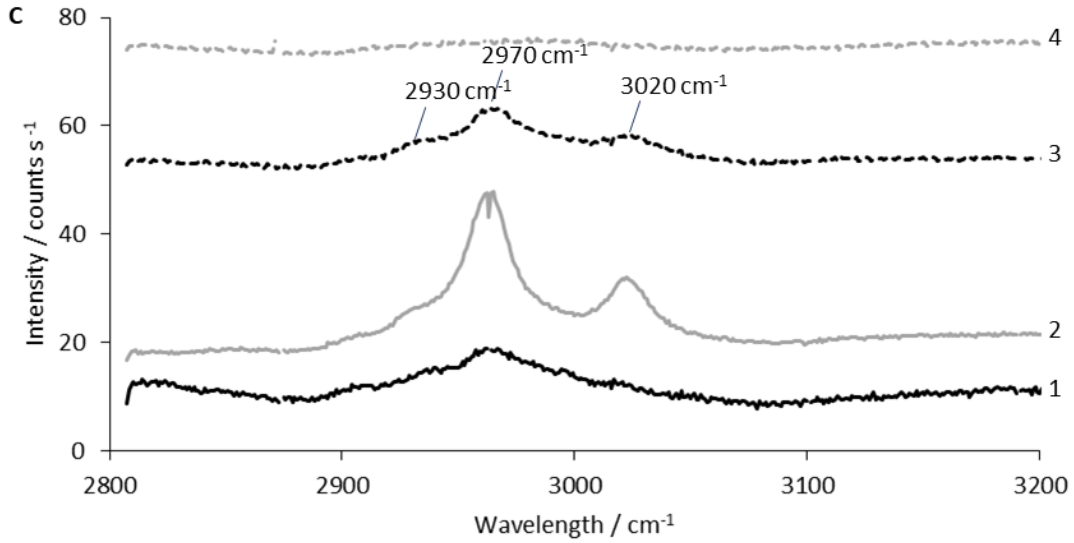

Figure 3.39 .TIR Raman spectra for 1- a clean silica wafer, 2- palladium/OAm nps LB deposited onto a silica wafer, 3- palladium/OAm nps LB deposited onto a silica wafer plasma cleaned for 20 s, 4- palladium/OAm nps LB deposited onto a silica wafer plasma cleaned for 60 s. Spectra taken (Figure 3.38 A-B, Figure 3.39 A) across three differing regions of wavelength, *with 532 nm excitation wavelength. All spectra were offset for clarity. Single point data, attributed to stray electronic signals, have been removed as part of data processing.*

3.7. Conclusions

Monodisperse nanoparticles with controlled particle size and uniform shape, were synthesised for a range of metal and capping agent combinations. LB trough deposition allowed for the subsequent formation of uniform and tightly packed nanoparticle films. TIR Raman monitoring for a variety of capped nanoparticles, gave initial proof of concept of the ability of the technique to detect small amounts of organic moieties at a nanoparticles catalyst surface. This was the case not only for silver nanoparticles (where SERS activity likely contributes to the signal seen), but also for SERS inactive palladium nanoparticles. Plasma cleaning allowed validation of assignment of spectral bands to the organic capping agent and efficient cleaning of the surface in advance of *in situ* monitoring of nanoparticle catalysts

3.8. Bibliography

(1) Rylander, P. *Catalytic Hydrogenation over Platinum Metals*; Elsevier, 2012.

(2) Bratlie, K. M.; Lee, H.; Komvopoulos, K.; Yang, P.; Somorjai, G. A. Platinum Nanoparticle Shape Effects on Benzene Hydrogenation Selectivity. *Nano Lett.* **2007**, *7* (10), 3097–3101.

(3) Blaser, H. U.; Jalett, H. P.; Müller, M.; Studer, M. Enantioselective Hydrogenation of α-Ketoesters Using Cinchona Modified Platinum Catalysts and Related Systems: A Review. *Catal. Today* **1997**, *37* (4), 441–463.

(4) Zaera, F.; Somorjai, G. A. Hydrogenation of Ethylene over Platinum (111) Single-Crystal Surfaces. *J. Am. Chem. Soc.* **1984**, *106* (8), 2288–2293.

(5) Krier, J. M.; Michalak, W. D.; Baker, L. R.; An, K.; Komvopoulos, K.; Somorjai, G. A. Sum Frequency Generation Vibrational Spectroscopy of Colloidal Platinum Nanoparticle Catalysts: Disordering versus Removal of Organic Capping. *J. Phys. Chem. C* **2012**, *116* (33), 17540–17546.

(6) Bassett, G. A.; Menter, J. W.; Pashley, D. W. Moire Patterns on Electron Micrographs, and Their Application to the Study of Dislocations in Metals. *Proc. R. Soc. Math. Phys. Eng. Sci.* **1958**, *246* (1246), 345–368.

(7) Kawasaki, T.; Yoshida, T.; Matsuda, T.; Osakabe, N.; Tonomura, A.; Matsui, I.; Kitazawa, K. Fine Crystal Lattice Fringes Observed Using a Transmission Electron Microscope with 1 MeV Coherent Electron Waves. *Appl. Phys. Lett.* **2000**, *76* (10), 1342.

(8) Koski, K. J.; Kamp, N. M.; Smith, R. K.; Kunz, M.; Knight, J. K.; Alivisatos, A. P. Structural Distortions in 5–10 Nm Silver Nanoparticles under High Pressure. *Phys. Rev. B* **August 10**, *78* (16), 165410.

(9) Wagner, C. Theory of Aging and Precipitation through Dissolution-Ostwald Ripening. *Z Elektrochem* **1961**, *581*.

(10) Zhang, J. L.; Srivastava, R. S.; Misra, R. D. K. Core−Shell Magnetite Nanoparticles Surface Encapsulated with Smart Stimuli-Responsive Polymer: Synthesis, Characterization, and LCST of Viable Drug-Targeting Delivery System. *Langmuir* **2007**, *23* (11), 6342–6351.

(11) Shukla, N.; Liu, C.; Jones, P. M.; Weller, D. FTIR Study of Surfactant Bonding to FePt Nanoparticles. *J. Magn. Magn. Mater.* **2003**, *266* (1–2), 178–184.

(12) Buck, M. R.; Biacchi, A. J.; Schaak, R. E. Insights into the Thermal Decomposition of Co(II) Oleate for the Shape-Controlled Synthesis of Wurtzite-Type CoO Nanocrystals. *Chem. Mater.* **2014**, *26* (3), 1492–1499.

(13) Griffiths, P. C.; Fallis, I. A.; Willock, D. J.; Paul, A.; Barrie, C. L.; Griffiths, P. M.; Williams, G. M.; King, S. M.; Heenan, R. K.; Görgl, R. The Structure of Metallomicelles. *Chem. – Eur. J.* **2004**, *10* (8), 2022–2028.

(14) Stallforth, P.; Adibekian, A.; Seeberger, P. H. De Novo Synthesis of a D-Galacturonic Acid Thioglycoside as Key to the Total Synthesis of a Glycosphingolipid from Sphingomonas Yanoikuyae. *Org. Lett.* **2008**, *10* (8), 1573–1576.

(15) Miller, F. A.; Wilkins, C. H. Infrared Spectra and Characteristic Frequencies of Inorganic Ions. *Anal. Chem.* **1952**, *24* (8), 1253–1294.

(16) Mallick, K.; Witcomb, M. J.; Scurrell, M. S. Polyaniline Stabilized Highly Dispersed Gold Nanoparticle: An in-Situ Chemical Synthesis Route. *J. Mater. Sci.* **2006**, *41* (18), 6189–6192.

(17) Pimprikar, P. S.; Joshi, S. S.; Kumar, A. R.; Zinjarde, S. S.; Kulkarni, S. K. Influence of Biomass and Gold Salt Concentration on Nanoparticle Synthesis by the Tropical Marine Yeast Yarrowia Lipolytica NCIM 3589. *Colloids Surf. B Biointerfaces* **2009**, *74* (1), 309–316.

(18) Kapoor, S. Preparation, Characterization, and Surface Modification of Silver Particles. *Langmuir* **1998**, *14* (5), 1021–1025.

(19) He, R.; Qian, X.; Yin, J.; Zhu, Z. Preparation of Polychrome Silver Nanoparticles in Different Solvents. *J. Mater. Chem.* **2002**, *12* (12), 3783–3786.

(20) Novak, J. P.; Nickerson, C.; Franzen, S.; Feldheim, D. L. Purification of Molecularly Bridged Metal Nanoparticle Arrays by Centrifugation and Size Exclusion Chromatography. *Anal. Chem.* **2001**, *73* (23), 5758–5761.

(21) Wang, C.; Peng, S.; Chan, R.; Sun, S. Synthesis of AuAg Alloy Nanoparticles from Core/Shell-Structured Ag/Au. *Small* **2009**, *5* (5), 567–570.

(22) Leff, D. V.; Brandt, L.; Heath, J. R. Synthesis and Characterization of Hydrophobic, Organically-Soluble Gold Nanocrystals Functionalized with Primary Amines. *Langmuir* **1996**, *12* (20), 4723–4730.

(23) Mishra, T.; Sahu, R. K.; Lim, S. H.; Salamanca-Riba, L. G.; Bhattacharjee, S. Hexadecylamine Capped Silver and Gold Nanoparticles: Comparative Study on Formation and Self-Organization. *Mater. Chem. Phys.* **2010**, *123* (2–3), 540–545.

(24) Hou, Y.; Kondoh, H.; Ohta, T.; Gao, S. Size-Controlled Synthesis of Nickel Nanoparticles. *Appl. Surf. Sci.* **2005**, *241* (1–2), 218–222.

(25) Yang, J.; Lee, J. Y.; Too, H. P. Size Effect in Thiol and Amine Binding to Small Pt Nanoparticles. *Anal. Chim. Acta* **2006**, *571* (2), 206–210.

(26) Mazumder, V.; Sun, S. Oleylamine-Mediated Synthesis of Pd Nanoparticles for Catalytic Formic Acid Oxidation. *J. Am. Chem. Soc.* **2009**, *131* (13), 4588–4589.

(27) Iablokov, V.; Beaumont, S. K.; Alayoglu, S.; Pushkarev, V. V.; Specht, C.; Gao, J.; Alivisatos, A. P.; Kruse, N.; Somorjai, G. A. Size-Controlled Model Co Nanoparticle Catalysts for CO_2 Hydrogenation: Synthesis, Characterization, and Catalytic Reactions. *Nano Lett.* **2012**, *12* (6), 3091–3096.

(28) Chesman, A. S. R.; Duffy, N. W.; Peacock, S.; Waddington, L.; Webster, N. A. S.; Jasieniak, J. J. Non-Injection Synthesis of Cu_2ZnSnS_4 Nanocrystals Using a Binary Precursor and Ligand Approach. *RSC Adv.* **2012**, *3* (4), 1017–1020.

(29) Zhang, Y.; Grass, M. E.; Habas, S. E.; Tao, F.; Zhang, T.; Yang, P.; Somorjai, G. A. One-Step Polyol Synthesis and Langmuir−Blodgett Monolayer Formation of Size-Tunable Monodisperse Rhodium Nanocrystals with Catalytically Active (111) Surface Structures. *J. Phys. Chem. C* **2007**, *111* (33), 12243–12253.

(30) Morita, M.; Ohmi, T.; Hasegawa, E.; Kawakami, M.; Ohwada, M. Growth of Native Oxide on a Silicon Surface. *J. Appl. Phys.* **1990**, *68* (3), 1272–1281.

(31) Borodko, Y.; Habas, S. E.; Koebel, M.; Yang, P.; Frei, H.; Somorjai, G. A. Probing the Interaction of Poly(vinylpyrrolidone) with Platinum Nanocrystals by UV−Raman and FTIR. *J. Phys. Chem. B* **2006**, *110* (46), 23052–23059.

(32) Xia, X.; Zeng, J.; Oetjen, L. K.; Li, Q.; Xia, Y. Quantitative Analysis of the Role Played by Poly(vinylpyrrolidone) in Seed-Mediated Growth of Ag Nanocrystals. *J. Am. Chem. Soc.* **2012**, *134* (3), 1793–1801.

(33) Dutta, K.; Brar, A. S. Poly(vinylpyrrolidone): Configurational Assignments by One- and Two-Dimensional NMR Spectroscopy. *J. Polym. Sci. Part Polym. Chem.* **1999**, *37* (21), 3922–3928.

(34) Dutta, K.; Brar, A. S. Poly(vinylpyrrolidone): Configurational Assignments by One- and Two-Dimensional NMR Spectroscopy. *J. Polym. Sci. Part Polym. Chem.* **1999**, *37* (21), 3922–3928.

(35) Wang, W.; Wang, A. Synthesis and Swelling Properties of pH-Sensitive Semi-IPN Superabsorbent Hydrogels Based on Sodium Alginate-G-Poly(sodium Acrylate) and Polyvinylpyrrolidone. *Carbohydr. Polym.* **2010**, *80* (4), 1028–1036.

(36) Duff, D. G.; Edwards, P. P.; Johnson, B. F. G. Formation of a Polymer-Protected Platinum Sol: A New Understanding of the Parameters Controlling Morphology. *J. Phys. Chem.* **1995**, *99* (43), 15934–15944.

(37) Born, M.; Wolf, E. *Principles of Optics, 7th Exp. Ed*; Cambridge University Press, 1999.

(38) Mie, G. Beiträge zur Optik trüber Medien, speziell kolloidaler Metallösungen. *Ann. Phys.* **1908**, *330* (3), 377–445.

(39) Bergius, W. N. A.; Hutchings, L. R.; Sarih, N. M.; Thompson, R. L.; Jeschke, M.; Fisher, R. Synthesis and Characterisation of End-Functionalised poly(N-Vinylpyrrolidone) Additives by Reversible Addition–fragmentation Transfer Polymerisation. *Polym. Chem.* **2013**, *4* (9), 2815.

(40) Schmidt, W. F.; Mookherji, S.; Crawford, M. A. Unit Cell Volume and Liquid-Phase Immiscibility in Oleate–stearate Lipid Mixtures. *Chem. Phys. Lipids* **2009**, *158* (1), 10–15.

(41) Emory, S. R.; Haskins, W. E.; Nie, S. Direct Observation of Size-Dependent Optical Enhancement in Single Metal Nanoparticles. *J. Am. Chem. Soc.* **1998**, *120* (31), 8009–8010.